Subcortical circuit dysfunctions delay perceptual decision-making in autism models

Laura E. Burnett[1], Peter Koppensteiner[1], Olga Symonova[1], Tomás Masson[1], Tomas Vega-Zuniga[1], Ximena Contreras[1], Thomas Rülicke[2], Ryuichi Shigemoto[1], Gaia Novarino[1], Maximilian Jösch[1*].

[1] Institute of Science and Technology Austria; Am Campus 1, 3400 Klosterneuburg, Austria.

[2] Institute of Laboratory Animal Science, University of Veterinary Medicine Vienna; Veterinärplatz 1, 1210 Vienna, Austria.

[*]Correspondance: maxjosch@ist.ac.at

Abstract

Autism spectrum disorders (ASD) include a range of neurodevelopmental conditions[1], often co-occurring with sensory processing abnormalities[2,3]. The neural origins of these impairments are thought to reside in cortical circuits[4–6], affecting perception and decision-making[3]. Here we demonstrate that efficient and timely responses to visual threats are disrupted across ASD mouse models, despite differences in their underlying molecular mechanisms. These delays in perceptual decision-making (PDM) to visual threats are due to cognitive, not sensory or motor impairments and are linked to reduced fear memory. Optogenetic perturbation and electrophysiological experiments revealed a potassium-channel mediated hypoexcitability phenotype in a subcortical node, the dorsal periaqueductal grey (dPAG). *In vivo* pharmacological rescue of dPAG hypoexcitability reverses both delayed PDM and fear memory, emphasising the role of timely perception in ASDs and learning in general. Our work underscores the significance of perception and subcortical pathways in ASD, providing a behavioural biomarker to bridge molecules, circuits and behaviour.

Introduction

Autism spectrum disorders (ASD) are conditions characterised by challenges with social interactions and repetitive behaviours, reflected in inadequate responses to others' mental states and emotions[1]. These alterations in social cognition co-occur with disordered sensory processing[2], a widespread yet often overlooked feature across ASD observed in every sensory modality[3]. In the visual domain, affected individuals frequently exhibit difficulties with visual attention and hyper- or hyposensitivity to visual stimuli[7], and mounting evidence suggests that the circuits involved in visual information processing are disrupted[8]. For example, atypical neuronal responses to faces and looming stimuli have been observed in individuals with ASD[9–11]. Such sensory deficits directly affect visually-guided behaviours such as gaze control, which emerges at a few months of age[12] and forms a prominent diagnostic feature[13]. Changes in gaze dynamics to subliminal stimuli[14] indicate that neuronal circuits mediating subconscious visual responses are affected, pointing towards subcortical circuits, particularly the superior colliculus (SC)[8,15,16].

Deficits in sensation are seemingly separate phenomena from the more studied cognitive impairments in ASD, believed to arise from cortical malfunctions[4–6]. However, their close association is indicative of the possibility of a common underlying thread. Such evidence has recently implicated SC-pathway impairments with atypical sensory and cognitive processing[8,16]. Given this evidence, we decided to directly explore the relationship between sensation and cognition in ASD within an innate, robust and reproducible sensorimotor transformation known to be mediated by the SC - the looming escape response (LER) [17,18]. Using *Setd5*[19] as a case study, we show that the LER is impaired, not due to direct sensory nor motor deficits. While all animals immediately detect the looming stimulus and can respond vigorously to a threat, they require longer to initiate the escape response than their wild-type siblings and are incapable of forming a fear or place avoidance memory. These deficits emerge through changes in the intrinsic excitability due to an increased potassium channel conductance of neurons in the dorsal periaqueductal grey (dPAG), a structure known for commanding escape responses and to receive direct input from the SC[20,21]. Rescuing this hypoexcitability phenotype in the dPAG, recovers their behavioural deficits and memory formation, linking a sensorimotor disorder via a defined molecular mechanism to cognitive dysfunction and associating the dPAG with ASD. Finally, we show that molecularly distinct ASD mouse models (*Cul3*[22] and *Ptchd1*[23]) present convergent behavioural deficits, similar to *Setd5*[19], but through distinct molecular pathways, indicating deficiencies in the dPAG and other subcortical pathways are instrumental in the emergence of conditions associated to ASDs.

Results

Delayed looming escape responses

To investigate whether subcortical visual circuits could be affected in mouse models of ASD, we evaluated the behavioural responses to the innate looming escape response (LER) paradigm. LER is largely independent of cortical input, requiring the SC and its downstream targets to initiate appropriate responses. For this purpose, we tested a genetic ASD mouse model affecting the *SET-domain containing 5 (Setd5)*[19], a histone-associated protein that has been found in ~1 % of patients with intellectual disability and ASD[19]. We subjected mutants (i.e., *Setd5*$^{+/-}$) and their wild-type (WT) siblings to our LER paradigm, where mice would automatically trigger a sequence of five consecutive looms upon entering a threat zone (Fig. 1a, see methods). For all experiments, we only used animals without any eye abnormalities, which are described to sometimes occur in *Setd5* mutant animals[19]. During the acclimatisation period, all animals showed similar exploratory behaviour and dynamics (Supplementary Fig. 1a-g), and seemingly similar behavioural responses, escaping to the shelter upon stimulus presentation (Suppl. Video 1). However, behavioural differences between the genotypes became evident when observing their reaction times (Fig. 1b). While WT siblings responded robustly to the first stimulus presentation, their heterozygous siblings required, on average, more repetitions to elicit an escape response (Fig. 1c), had longer reaction times between the stimulus start and the maximum speed, and escaped with less vigour, as represented by their maximal speed[24] (Fig. 1f). This difference in response reaction time is an intrinsic and not an adaptive property since it is present during the first loom presentation (Fig. 1g,

left). The differences across genotypes were robust across trials and days (Extended Data Fig. 1f-g) and independent of the location, head direction, speed of the animal at stimulus onset (Supplementary Fig. 1h-k), or sex (Fig. 1b-g - females, and Extended Data Fig. 1b-d - males). The maximal speeds during the first loom were indistinguishable among genotypes, despite having different reaction times (Fig. 1g, right). This indicates that the escape delay differences are not due to intrinsic motor problems, but emerge due to perceptual decision-making deficits - the process of extracting and integrating sensory information to subsequently initiate an action. These results show that the LER can serve as a robust behavioural assay to uncover the underlying circuit dysfunctions across ASD models.

To test whether the delay in initiating an escape to the loom was due to the mutant mice simply detecting the stimulus later than their WT siblings, we examined the immediate change in the speed of the animals from the time of the first loom, selecting only the trials where the mice performed an escape to the shelter at any point during the looming events. As expected, WT animals showed mainly an increase in speed immediately following the stimulus onset. In contrast, in mutant animals we saw a marked increase in arrest behaviour immediately following the appearance of the stimulus (Fig. 1c-e, Extended Data Fig. 1a), indicating that *Setd5*$^{+/-}$ animals detected a stimulus change within a similar timeframe to their WT littermates. This arrest behaviour is not the known freezing behaviour, another commonly observed response to the looming stimulus characterised by the complete lack of any movement over an extended time period. Instead, during the arrest, animals can still make small and slow movements of the head and upper body (see Supplementary Videos), a behaviour that is indicative of an ongoing evaluation of the threat level as previously shown for loom stimuli of different contrast[24]. This suggests that the delay in LER arises from difficulties in either evaluating the threat level of the stimulus or in initiating an appropriate response.

Given that cortical malfunctions have been suggested as the cause of sensory differences in autism[4–6] and that the visual cortex has been shown to modulate the response magnitude of looming sensitive cells in the SC[25], we tested whether the behavioural responses are affected in cortex and hippocampus-specific conditional *Setd5* animals (*Setd5*$^{+/fl}$; *Emx1*-Cre, Extended Data Fig. 2). These animals showed no behavioural differences in their reaction times, vigour, or response kinetics (Extended Data Fig. 2c-f), indicating that subcortical pathways, namely the SC and PAG, and not cortical areas are in dysfunction.

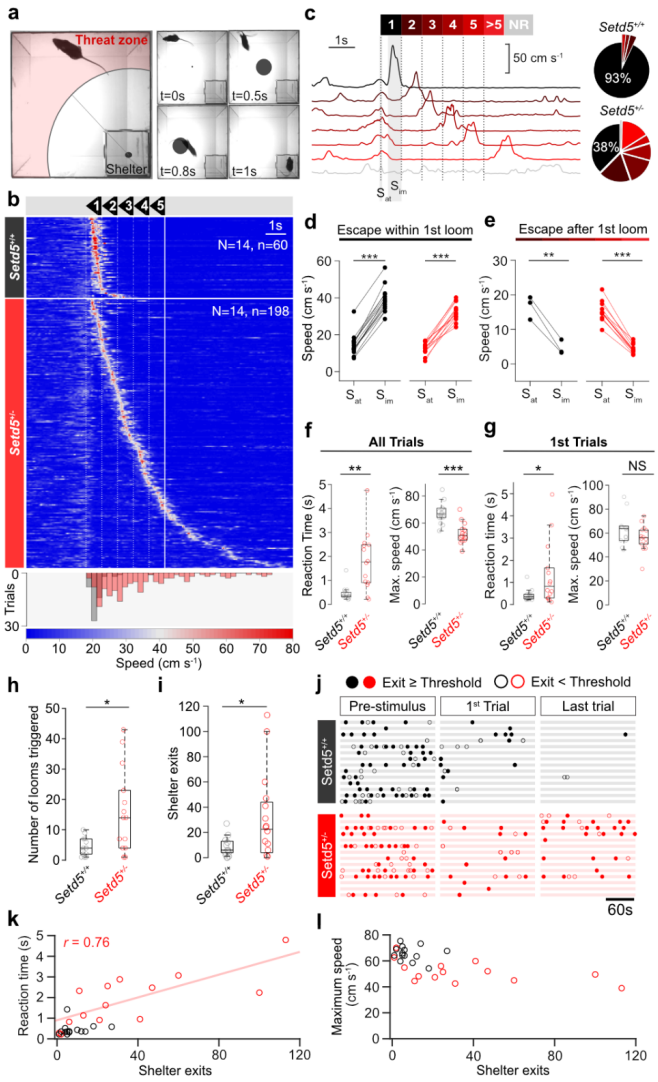

Figure 1. ASD mice exhibit delayed and less vigorous looming escape responses. a, Left, video frame from a single trial of the looming escape response (LER) paradigm showing the location of the shelter and the threat zone. Right, video frames from a trial, covering one second after the triggering of the looming stimulus, t = 0 s. **b**, Top, raster plot of mouse speed in response to the looming stimuli (white, dotted vertical lines denote the start of each loom; solid white line denotes the end of the stimulus) for *Setd5*$^{+/+}$ (upper, 60 trials) and *Setd5*$^{+/-}$ (lower, 198 trials), sorted by reaction time. Bottom, distribution of reaction times for all *Setd5*$^{+/+}$ (black) and *Setd5*$^{+/-}$ (red) trials, $p < 0.001$. **c**, Left, single trial traces from each category based on whether the mouse responds within 1 of the 5-loom stimuli, after the 5th (>5), or not at all (NR - no response) from one *Setd5*$^{+/-}$ mouse. Grey shaded areas represent the frames over which the speed at the start of the stimulus (S_{at}) and the immediate response speed (S_{im}) are calculated. Right, proportion of trials where the mice respond within each of the seven categories for *Setd5*$^{+/+}$ (top) and *Setd5*$^{+/-}$ (bottom), $p < 0.001$. **d**, Speed change immediately following the stimulus presentation for trials where the mice escape within the first loom presentation (left, *Setd5*$^{+/+}$, n = 14, black, $p < 0.001$, paired *t*-test; right, *Setd5*$^{+/-}$, n = 14, red, $p < 0.001$, paired *t*-test). **e**, Speed change immediately following the first loom for trials where the mice escape during or after the second loom (left, *Setd5*$^{+/+}$, n = 3, black, $p = 0.007$, paired *t*-test; right, *Setd5*$^{+/-}$, n = 11, red, $p < 0.001$,

paired *t*-test). **f**, Mean reaction time (left) and maximum escape speed (right) per animal, for all trials where the mice escaped (reaction time, P = 0.001; maximum escape speed, P < 0.001). **g**, Mean reaction time (left) and maximum escape speed (right) per animal, for the first ever loom presentations (reaction time, P = 0.046; maximum escape speed, P = 0.166). **h**, Summary of total looms triggered per genotype across 5 days of testing (*Setd5*$^{+/+}$, 4.36 looms; *Setd5*$^{+/-}$, 16 looms, P = 0.013). **i**, Total shelter exits across the 5 test days (*Setd5*$^{+/+}$, 6.0; *Setd5*$^{+/-}$, 24.5, P = 0.019). **j**, Exploratory shelter exit behaviour during the pre-stimulus acclimatisation, first and last trial of the LER paradigm. Each row represents one animal, filled and open dots represent exits into the threat zone or not, respectively. **k**, Relationship between the number of shelter exits and the average reaction time per animal (*Setd5*$^{+/+}$, p = 0.626; *Setd5*$^{+/-}$, *r* = 0.76, p = 0.002, Pearson's correlation). **l**, Relationship between the number of shelter exits and the maximum escape speed per animal (*Setd5*$^{+/+}$, p = 0.547; *Setd5*$^{+/-}$, p = 0.053, Pearson's correlation). Box-and-whisker plots show median, IQR and range. P-values: Wilcoxon's test, p-values: two-sample Kolmogorov-smirnov test, unless specified. For detailed statistics, see Supplementary Table 1.

Repetitive looming escape responses

Although the innate LER does not require learning, repeated loom presentations cause adaptive behavioural changes, for example, the emergence of fear memory of the threat zone[24]. Given that *Setd5*$^{+/-}$ triggered three times more looming events and shelter exits than their WT siblings (Fig. 1h,i, Extended Data Fig. 1e), we explored if altered adaptation to repeated presentations could account for the observed difference in average reaction time and vigour (Fig. 1f). For that purpose, we compared the intrinsic behavioural characteristics and the effect of the LER on the exploration strategies and behavioural adaptations across days (Fig. 1j, Extended Data Fig. 1e-j). Before stimulus exposure, both genotypes traversed the arena, left the shelter, and remained outside of the shelter for similar extents of time (Supplementary Fig. 1c-g & Extended Data Fig. 1h-j (day 0)), indicating that their innate exploration strategies cannot account for the differences in reaction time and vigour. WT animals showed expected reductions in their exploratory behaviour following the initial exposure to the looming stimulus, staying closer, making fewer exits, and staying outside of the shelter for a shorter period than during the pre-stimulus exploration time (Extended Data Fig. 1h-j), eliciting fewer looms in total (Extended Data Fig. 1e) with relatively constant reaction time and response vigour (Extended Data Fig. 1f-g). Strikingly, *Setd5*$^{+/-}$ consistently triggered more looms and had no signs of sensitisation upon repeated exposures (Extended Data Fig. 1e-j). After the initial decrease in exploration following the first stimulus presentation, they showed no further consolidation of fear memory to the threat zone (Extended Data Fig. 1h-j). The reaction time and vigour of the escape response remained longer and slower across days (Extended Data Fig. 1f-g), respectively, indicating that *Setd5*$^{+/-}$ do not sensitise as their WT siblings do to the LER paradigm. Importantly, the reaction time, but not the escape vigour, was different at the very first presentation of the looming stimulus (Fig. 1g), showing that the differences in LER are mediated by intrinsic factors, whereas differences in response vigour arise due to adaptation of the response. We next tested if the delayed perceptual decisions (Fig.1) are related to the consolidation of fear memory (Fig. 1j, Extended Data Fig. 1h-j), two seemingly independent behaviours. We analysed the average number of shelter exits for each animal and compared them with their average reaction times and vigour (Fig. 1k-l). Surprisingly, the strength of the fear memory was a strong predictor of the

reaction times, but not vigour, suggesting that the timing of the perceptual decision and the formation of fear memory are intrinsically linked. To assess the limits of response adaptation and to ascertain if the presence of a reward would overcome the fear, we conducted the same behavioural experiment but with the presence of a food reward on the far side of the arena within the threat zone (Extended Data Fig. 1k), and with no inter-stimulus interval restriction. Although WT siblings did make some attempts to retrieve the food reward, they quickly sensitised, rarely leaving the shelter and were unsuccessful in obtaining the food reward. *Setd5*$^{+/-}$, on the other hand, increased their shelter leaving events, in many cases persisting until reaching the reward (Extended Data Fig. 1l-m, Suppl. Video 2). Despite the rapid and repeated exposure, Setd5$^{+/-}$ mice continued to escape to the shelter upon stimulus presentation, for >20 consecutive presentations, with their reaction times mildly adapting (Extended Data Fig. 1n, top) and vigour remaining largely constant (Extended Data Fig. 1n, bottom), indicating that differences in response vigour do not arise over repeated consecutive exposures.

Intact visual response properties in Setd5$^{+/-}$

Changes in average reaction times have previously been shown to depend on the saliency of the threat stimulus. Whereas repeated high-contrast looming stimuli evoke strong LER, low-contrast looms drive less vigorous escapes and longer reaction times[24], suggesting that deficits in visual processing could underlie the behavioural disorders observed in *Setd5*$^{+/-}$. This possibility is aggravated by the fact that the expression of genes involved in eye development are known to be misregulated in *Setd5*$^{+/-}$ animals[19]. To explore possible visual response changes, we recorded visually-evoked responses across different layers of the SC, using 32-channel silicon probes in head-fixed, awake-behaving animals (Fig. 2a), and determined the recording depth using current source density analysis (Fig. 2b-c). In our setup, mutant and control animals had similar running probabilities and showed similar baseline firing properties (Fig. 2d). We next assessed visual response properties to full-field flashes, visual stimuli that drive all neurons similarly irrespective of their receptive field positions. First, we show that pupil dynamics are unaffected across genotypes (Fig. 2e). Next, when clustering visually responsive cells into 10 clearly defined groups, we could observe similar relative proportions and identical response properties (Fig. 2f-g). Identical responses were also observed in their spatio-temporal receptive fields as well as the proportion of ON and OFF-responsive cells (Extended Data Fig. 3a-g). Direction-selective responses, either to bars or gratings (Extended Data Fig. 3h-m), were also indistinguishable across groups. Finally, we explored the response properties to looming stimuli across SC layers. Looms elicit robust and reproducible firing across genotypes (Fig. 2h), with similar firing, peak rates and time-to-peak responses across genotypes (Fig. 2i-k). The overall response kinetics (Fig. 2l) as well as the adaptation in average firing rates across presentations (Fig. 2m,n) were indistinguishable across genotypes. The lack of any reportable visual response difference across the SC layers indicates that retino-colliculuar visual processing is largely unaltered and excludes the possibility that sensory processing can account for the observed visuomotor deficits.

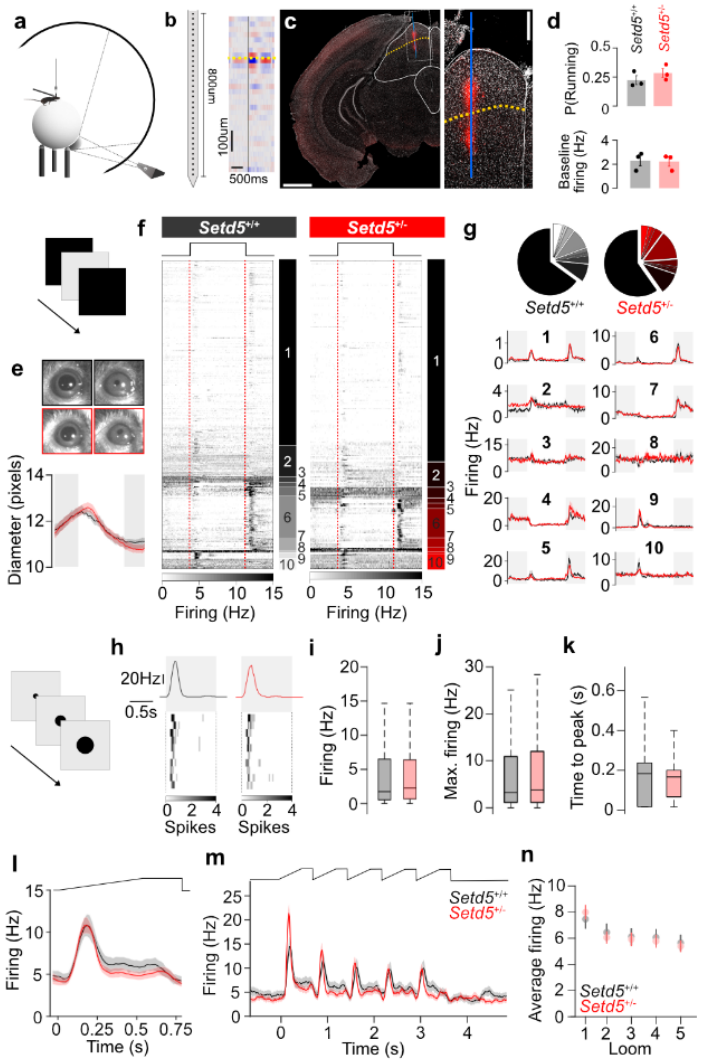

Figure 2. Intact visual processing across the SC. a, Schematic of the *in vivo* recording setup displaying the spherical treadmill and light projector illuminating the spherical screen. **b**, Left, Schematic of the 32-channel silicon probe used to record extracellular activity aligned with the current source density analysis of a single flash stimulus averaged over 10 presentations. Black vertical line represents the stimulus onset, yellow dotted line marks the inflection depth separating the current source and sink. **c**, Histological reconstruction of the probe position marked with DiI (120 µm coronal section, scale bar: 1000 µm) with a close-up (scale bar: 250 µm). Yellow dotted line as in (**b**). **d**, Proportion of time the mice were moving during the recording sessions (P = 0.400, top) and SC's baseline firing rate (P = 0.880, bottom). **e**, Pupil dilation in response to the full-field flash stimulus. Example images of dilated and constricted pupils in responses to the OFF (left) and ON (right) periods of the flash. Setd5$^{+/+}$ (black), Setd5$^{+/-}$ (red) (P = 0.060). **f**, Sorted raster plot of neural responses to a single flash stimulus. Vertical red dotted lines indicate the on and offset of the flash stimulus. **g**, Proportion of cells in each cluster (top). Mean ± s.e.m. of the flash responses in each cluster (traces). **h**, Mean and spike raster plots from single Setd5$^{+/+}$ (black) and Setd5$^{+/-}$ (red) units to 10 repetitions of a single loom stimulus. **i-k**, Summary of mean, maximum and time-to-peak firing (**i**, P = 0.215; **j**, P = 0.100; **k**, P = 0.372). **l**, Mean±s.e.m. response of all and (**m**) of the 5 consecutive loom stimuli for Setd5$^{+/+}$ (black) and Setd5$^{+/-}$ (red) units. **n**, Average firing to a single loom across the 5-loom stimulus (p = 0.732) Box-and-whisker plots show

median, IQR and range. P-values: Wilcoxon's test, p-values: two-way repeated measures ANOVA, unless specified. For detailed statistics, see Supplementary Table 1.

Optogenetic stimulation of deep medial SC replicates response delay

The lack of sensory response differences in the SC suggests that the main cause of the behavioural difference may reside in downstream areas. Given that the dorsal periaqueductal grey (dPAG) encodes for the choice of escape and controls the escape vigour[24], we hypothesised that optogenetic stimulation of the dPAG projecting SC cells should recapitulate some of the described behavioural differences observed in the *Setd5*$^{+/-}$. To test this, we focused on the *Setd5* mouse line and used unilateral *in vivo* channelrhodopsin-2 (ChR2) activation of VGluT2^{+} cells in the deep medial SC (dmSC) (Fig. 3a-c). In line with previous findings, activation of dmSC neurons in *Setd5*$^{+/+}$ animals instructed immediate shelter-directed escapes (Fig. 3d,f) and were absent in controls (Extended Data Fig. 4). Gradually increasing the laser power and thus, optogenetic activation, led to corresponding increases in the escape probability (Fig. 3i), the escape vigour (Fig. 3j) and decreases in the latency to respond (Fig. 3k). By contrast, activation of dmSC neurons in the *Setd5*$^{+/-}$ background, more often resulted in an initial arrest, followed by shelter seeking escape responses (Fig. 3e,f), mimicking the behavioural divergence observed for LER (Fig. 1). Interestingly, this behavioural difference was evident only during strong optogenetic activations. At lower laser intensities, both genotypes exhibited a transition from arrest to weak escape behaviours (Fig. 3f-h,l) with similarly low vigour (Fig. 3j) and reaction time (Fig. 3k). Given that changes in the strength of optogenetic activation mimic LER to looms of different contrast[24], we hypothesised that when probing animals to LER of different contrasts, both genotypes should show similar responses at lower contrast (Fig. 3m). For this purpose, we tested the LER to three different contrast levels: 98 %, 50 % and 20 % (Fig. 3n-p). As predicted, the LER to low-contrast looms did not differ across genotypes, showing similar response speeds (Fig. 3o) and reaction times (Fig. 3n). Remarkably, in *Setd5*$^{+/-}$ animals, these parameters remained constant across contrast levels, only the escape probability increased (Fig. 3p). This suggests that action initiation mechanisms, and not visual transformations, are disrupted. Overall, these results emphasise that the differences observed in this behaviour are mediated by altered processing downstream of the dmSC.

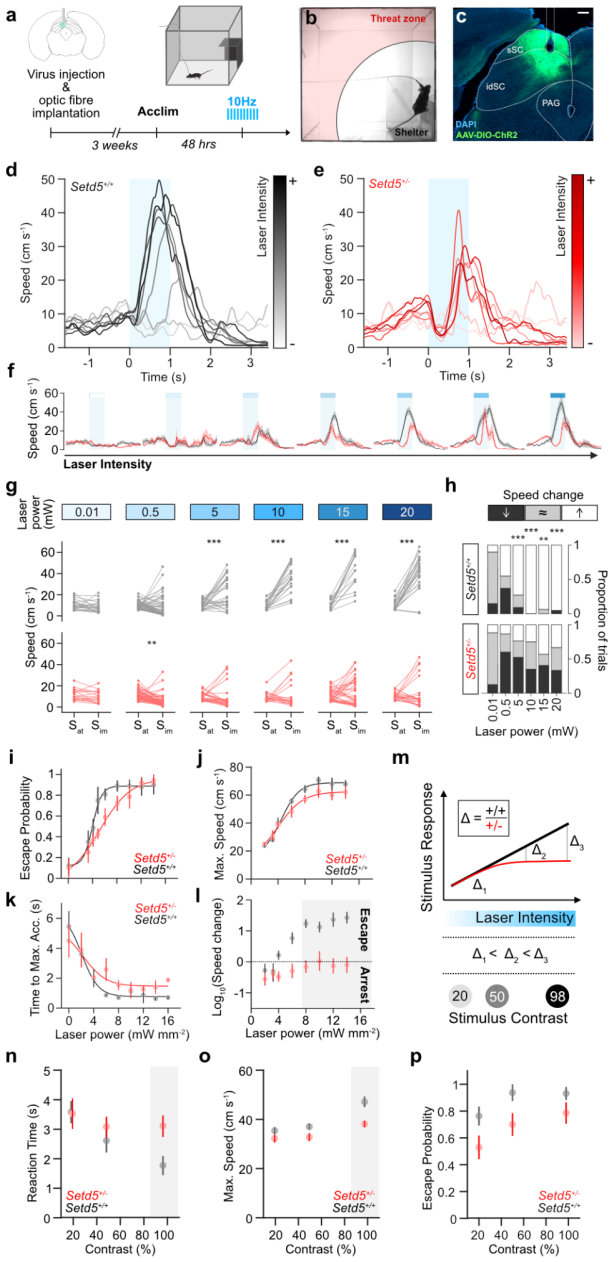

Figure 3. Optogenetic activation of deep SC neurons recapitulates LER differences. **a**, Schematic of ChR2 expression in the dmSC and implantation of the optic fibre, and timeline of the optogenetics experiments. **b**, Video frame during an optogenetics trial. **c**, Confocal micrograph of AAV-ChR2 expression in mSC and optic fibre location reconstruction. Scale bar: 200 µm. **d**-**e**, Mean speed responses to optogenetic stimulation at increasing laser intensities for *Setd5*$^{+/+}$ (**d**) and *Setd5*$^{+/-}$ (**e**) mice. Blue shaded areas represent the laser stimulation. **f**, Subplots of trials in (**d**-**e**) showing the mean and s.e.m of all trials at each intensity (l-r, low to high intensity). **g**, Change in speed upon light activation at different laser intensities for *Setd5*$^{+/+}$ (top, n = 4, 0.01mW mm^{-2}: p = 0.540, 18 trials; 0.5 mW mm^{-2}: p = 0.193, 51 trials; 5.0 mW mm^{-2}: p < 0.001, 22 trials; 10.0 mW mm^{-2}: p < 0.001, 22 trials; 15.0 mW mm^{-2}: p < 0.001, 16 trials; 20.0 mW mm^{-2}: p < 0.001, 21 trials, paired *t*-tests) and *Setd5*$^{+/-}$ (bottom, n = 4, 0.01mW mm^{-2}: p = 0.804, 17 trials; 0.5 mW mm^{-2}: p < 0.001, 60 trials; 5.0 mW mm^{-2}: p = 0.030, 28 trials; 10.0 mW mm^{-2}: p = 0.057, 27 trials; 15.0 mW mm^{-2}: p = 0.812, 45 trials; 20.0

mW mm^{-2}: p = 0.322, 28 trials, paired Wilcoxon's tests) optogenetics trials. **h**, Proportion of trials at different laser intensities that either show >1 standard deviation (SD) increase (white), >1 SD decrease (black) or <1 SD (grey) change in speed with light activation. Difference in distribution of responses between *Setd5*$^{+/+}$ and *Setd5*$^{+/-}$ at different laser intensities (0.01mW mm^{-2}: p = 0.649; 0.5 mW mm^{-2}: p = 0.193; 5.0 mW mm^{-2}: p < 0.001; 10.0 mW mm^{-2}: p < 0.001; 15.0 mW mm^{-2}: p = 0.004; 20.0 mW mm^{-2}: p < 0.001, Chi-Square tests). **i-l**, Psychometric, vigour and chronometric curves (**i,** Setd5$^{+/+}$, 312 trials, n = 4, slope=4.62, 95% confidence interval (2.87, 6.37); Setd5$^{+/-}$, 291 trials, n = 4, slope = 1.36, 95 % confidence interval (0.62, 2.11); **j**, Setd5$^{+/+}$, 195 trials, n = 4, slope = 2.63, 95 % confidence interval (0.90, 4.36); Setd5$^{+/-}$, 171 trials, n = 4, slope = 1.88, 95 % confidence interval (0.44, 3.31); **k**, Setd5$^{+/+}$: 195 trials, n=4, slope = 2.58, 95 % confidence interval (0.94, 4.22); Setd5$^{+/-}$, 171 trials, n = 4, slope = 1.88, 95 % confidence interval (-1.99, 5.76). **l**, Mean ± s.e.m. of the change in speed ($\log_{10}(Sp_{im}/Sp_{at})$) at different intensities (between genotype distributions: p < 0.001; grey area denotes statistically significant difference through multiple comparisons test). **m**, Schematic of the behavioural divergence between genotypes with increasing stimulus intensity (laser or loom). **i-k**, Summary of mean ± s.e.m. of (**n**) reaction time, (**0**) vigour, and (**p**) escape probability responses to the LER paradigm at different stimulus contrasts. (**n**, between genotypes: p < 0.001, between contrast: p = 0.003, **o,** between genotypes: p = 0.021, between contrast: p = 0.015; **p**, between genotypes: p < 0.001, between contrast: p = 0.005; grey area denotes statistically significant difference through multiple comparisons test). Lines are sigmoidal fits pooled across trials from all mice and binned according to light intensities. Error bars and shaded areas represent s.e.m. p-values: repeated measures ANOVA with multiple comparisons with Bonferroni correction, unless specified. For detailed statistics, see Supplementary Table 1.

dPAG neurons are hypoexcitable in the Setd5 mouse model

Our previous results point toward the direct involvement of the dPAG in the delayed LER response (Fig. 2,3). To test if any synaptic or intrinsic properties of dPAG neurons are impaired, we performed whole-cell patch-clamp recordings in slices (Fig. 4a). First, using the same animals used for optogenetic stimulation *in vivo*, we tested if the synaptic properties of dmSC inputs to the dPAG are changed. 10 Hz *ex vivo* optogenetic activation elicited monosynaptic excitatory postsynaptic current (EPSC) with an average current of −244±9.65 pA in *Setd5*$^{+/+}$ and -228±11.8 pA in *Setd5*$^{+/-}$ (Fig. 4a,b), larger than previously reported[24]. At this frequency, repeated stimulations showed no facilitation in both genotypes (Fig. 4b), indicating that dmSC inputs to the dPAG are unaltered. Next, we explored spontaneous neurotransmission by recording sEPSCs (Extended Data Fig. 5b-e), supporting the view that the synaptic properties remain similar at a circuit level. Finally, we probed the intrinsic properties of dPAG neurons, classifying them as excitatory and inhibitory based on their baseline firing rate[26] (Extended Data Fig. 6). Although the membrane potential, input resistance, membrane constant, and capacitance were identical between genotypes (Fig. 4c), we observed a stark decrease in the ability of these cells to generate action potentials in response to injected current (Fig. 4d), without affecting the rheobase (Extended Data Fig. 5f). These changes were accompanied by changes in the spike shape of Setd5$^{+/-}$ animals (Fig. 4e,f) that showed slightly higher depolarisation, lower after-hyperpolarisation and slower rise dynamics in comparison to their WT siblings (Fig. 4g). Based on prior work we know that stronger dPAG activation leads to more vigorous escapes and that the underlying biophysical mechanisms depend on dPAG neuronal synaptic integration and excitability[24]. Thus, intrinsic excitability changes in excitatory neurons are a proxy of the expected escape strength. Remarkably, the response characteristics of dPAG neurons

in *Setd5*$^{+/+}$ *and Setd5*$^{+/-}$ match their behavioural differences (Figs. 1 & 3). At weak current-injections (Fig. 4d), optogenetic activation (Fig. 3d-l) or low contrast looms (Fig. 3n-o), both genotypes are indistinguishable from each other. However, at stronger current-injections, optogenetic activation or high contrast looms, *Setd5*$^{+/+}$ *and Setd5*$^{+/-}$ diverge, with an hypoexcitability phenotype for *Setd5*$^{+/-}$ (Fig. 4d) that matches the delay in LER for optogenetic (Fig. 3g,l) and visual (Figs. 1, 3n) activations. To determine if the hypoexcitability phenotype was a brain-wide phenomenon, we patched dmSC interneurons (Extended Data Fig. 5g-l). Here, we observed a weaker and statistically non-significant hypoexcitability trend, indicating that the strength of the effect is area specific but not ruling out other brain-wide deficiencies. In combination with previous work[24] and our optogenetic experiments (Fig. 3), these results suggest intrinsic deficits in the dPAG account, at least partly, for the delayed PDM phenotype (Fig. 1).

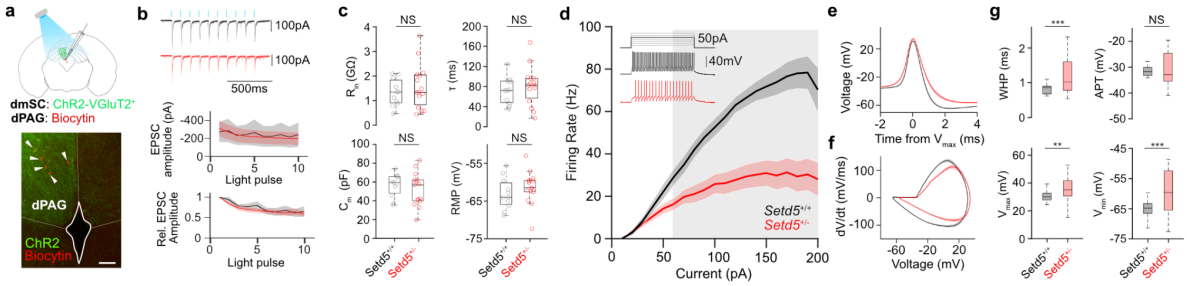

Fig. 4. *Setd5*$^{+/-}$ dPAG cells are hypoexcitable. a, Schematic of the experimental approach, *in vitro* patch clamp recordings (top) and micrograph of VGluT2^{+} dmSC projections to the dPAG infected with AAV9-ires-DIO-ChR2 (green) with dPAG biocytin filled and recorded cells (arrows, scale bar: 100 μm). **b**, Top, whole-cell voltage clamp traces of example *Setd5*$^{+/+}$ and *Setd5*$^{+/-}$ cells (black and red, respectively) responding to 10 Hz light stimulation (blue ticks). Amplitude (middle, $p = 0.078$) and relative EPSC amplitude (bottom, $p = 0.565$) of responses to sequential light pulses in a 10 Hz train. **c**, Intrinsic properties of *Setd5*$^{+/+}$ (n = 6, 11 cells) and *Setd5*$^{+/-}$ (n = 7, 14 cells) dPAG cells. Input resistance ($P = 0.756$, top left), membrane constant tau ($P = 0.436$, top right), membrane capacitance ($P > 0.995$, bottom left) and resting membrane potential ($P = 0.213$, bottom right). **d**, Summary of the relationship between current injection and action potential firing for putative glutamatergic cells showing a strong reduction in firing ($p < 0.001$). Inset, representative example traces to a 50 pA current injection. Grey area indicates the current injection values that significantly differ between *Setd5*$^{+/+}$ cells (black) and *Setd5*$^{+/-}$ cells (red) found by a multiple comparisons analysis with Tukey correction. **e**, Average shape and (**f**) phase plane analysis of the action potentials generated in the rheobase sweep (*Setd5*$^{+/+}$, 13 cells, 42 spikes; *Setd5*$^{+/-}$, 14 cells, 72 spikes). **g**, Action potential kinetics analysis. Top left: width at half-peak (WHP, $P < 0.001$); top right: action potential threshold (APT, $P = 0.821$); bottom left: action potential amplitude (V_{max}, $P = 0.003$); after-hyperpolarisation amplitude (V_{min}, $P < 0.001$). Box-and-whisker plots show median, IQR and range. P-values: Wilcoxon's test, p-values: two-way repeated measures ANOVA, unless specified.

dPAG cells are hypoexcitable due to K_v channel misregulation

Next, we investigated the underlying mechanisms of the hypoexcitable phenotype of the *Setd5*$^{+/-}$ PAG cells. The changes in excitability and spike kinetics are indicative of differences in channel composition that are part of adaptive homeostatic mechanisms[27], suggesting the influence of voltage-gated potassium channels (Kv). Previously published work[19], which studied the transcriptomic changes brought about by a mutation in *Setd5*$^{+/-}$*,* highlighted significant upregulation in the expression of Kv1.1. To test whether the blockade of Kv1.1 channels would rescue the hypoexcitability phenotype, we applied 100 nM of **α**-Dendrotoxin (**α**-DTX), a specific Kv1.1, Kv1.2 and Kv1.6 blocker, and patched dPAG cells. Strikingly, when we applied the same current steps to *Setd5*$^{+/-}$ cells in the presence of the Kv blocker, the spiking activity was rescued to levels similar to *Setd5*$^{+/+}$ both before and after drug application (Fig. 5a-d). In addition, after **α**-DTX application the spike dynamics remained identical in Setd5$^{+/+}$, whereas *Setd5*$^{+/-}$ became faster, mimicking the WT properties. These differences are not due to an overexpression of Kv1.1. Compared to other brain regions, the dPAG has a trend toward a reduction of the protein levels (Extended Data Fig. 5q-r), while protein distribution is not affected (Extended Data Fig. 5m-p). Kv1.1 has been recently shown to be involved in the homeostatic control of firing[27,28] through modulation of the axon initial segment (AIS)[29]. Thus, our behavioural and physiological results isolate a key molecular player in *Setd5,* Kv1.1*,* that causes the physiological hypoexcitability phenotype, probably arising through homeostatic misregulation, either by localisation[27], post-translational modifications[30] or interactions with auxiliary subunits[31]. These results suggest a novel drug target to reverse the delayed PDM phenotype and probe the causality of its correlation with fear memory deficits.

***In vivo* rescue of delayed perceptual decision-making and fear memory**

Our results indicate that the effects of excitability are not global but rather area-specific (Fig. 2, Fig. 5, Extended Data Fig. 5a-l). However, it is possible that other brain areas known to be involved in LER, such as the lateral amygdala or the lateral posterior thalamus (LP)[32], could also be changing their intrinsic excitability properties. To investigate whether dPAG hypoexcitability instructs delayed perceptual decision-making (PDM), we tested whether targeted **α**-DTX application to the dPAG could rescue the behavioural phenotype (Fig. 5e). We implanted cannulas above the dPAG in Setd5$^{+/-}$ and their WT littermates, an approach that was target-specific, as visualised through neurobiotin injections (Fig. 5f). Initially, we injected saline as a control in both cohorts and subsequently tested the LER (Fig. 5g). As previously demonstrated (Fig. 1), Setd5$^{+/-}$ animals responded slower than their WT littermates and had no difference in their maximal escape speed during the first presentation day (Fig. 5i,j). However, both cohorts' behaviours were indistinguishable from each other when **α**-DTX was applied, reacting immediately after the loom presentation (Fig. 5h-j, Suppl. Video 3). These findings are remarkable, as Setd5$^{+/-}$ animals are known to adapt across days (Extended Data Fig. 1f). We then quantified the shelter exits of both cohorts (Fig. 5k,l) to investigate whether the correlation between shelter exits and delayed PDM (Fig. 1k) could have a common origin. Interestingly, Setd5$^{+/-}$ animals also recovered their fear memory after **α**-DTX application, indicating that the timely initiation of actions and memory formation are closely linked. These results suggest that deficits in PDM can have far-reaching consequences for ASD.

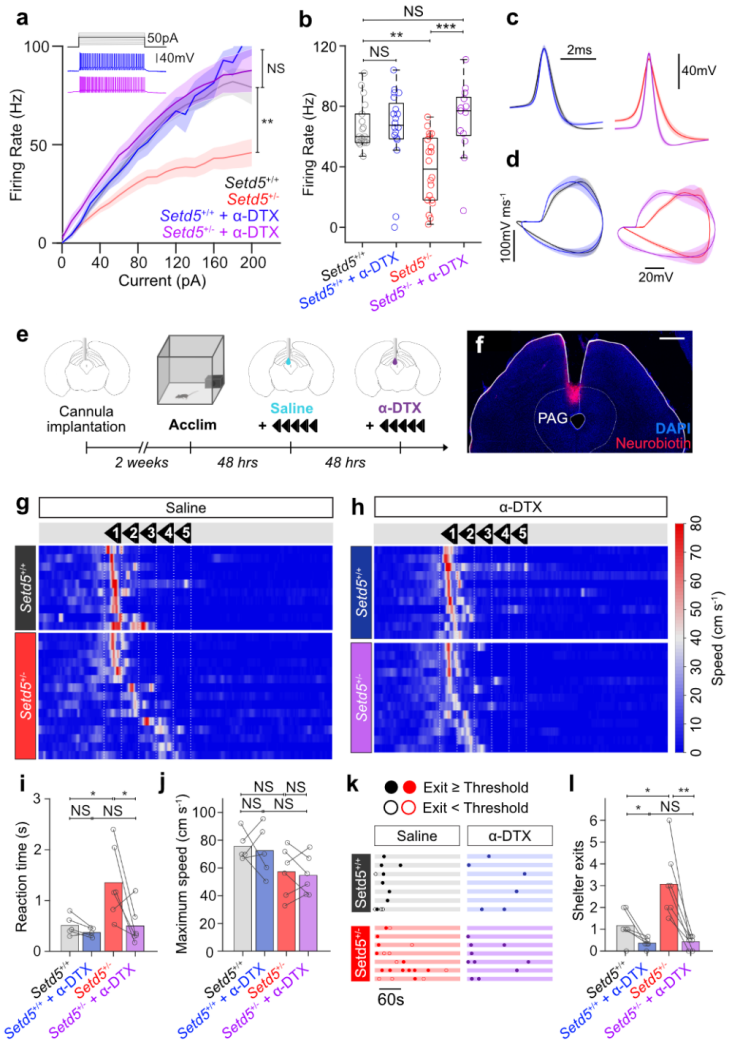

Fig. 5. Pharmacological Kv channel block rescues hypoexcitability, delayed LER and fear memory a, Summary of the relationship between current injection and action potential firing for all *Setd5*$^{+/+}$ cells (black, n = 18) and *Setd5*$^{+/-}$ cells (red, n = 20) before, and after (*Setd5*$^{+/+}$: blue, n =12 cells; *Setd5*$^{+/-}$: purple, n = 13 cells) application of α-Dendrotoxin (α-DTX, 100 nM), a Kv1.1, 1.2 and 1.6 blocker ($p > 0.995$ and $p = 0.0147$ for the effect of α-DTX on *Setd5*$^{+/+}$ and *Setd5*$^{+/-}$ firing, respectively). Inset, representative example traces from *Setd5*$^{+/+}$ cells (blue) and *Setd5*$^{+/-}$ (purple) cells after α-DTX application to a 50 pA current injection. **b**, Effect of α-DTX on firing in response to 120pA current injection. Before α-DTX (*Setd5*$^{+/+}$ versus *Setd5*$^{+/-}$; $p = 0.0017$), effect of α-DTX on *Setd5*$^{+/+}$ (before versus after α-DTX; $P > 0.995$) and *Setd5*$^{+/-}$ (before versus after α-DTX; $P < 0.001$, *Setd5*$^{+/+}$ before versus *Setd5*$^{+/-}$ after α-DTX; $P > 0.995$). Multiple comparison analysis after rm-ANOVA with Tukey correction. **c**, Action potential shape and **d**, phase plane analysis of the action potentials generated in the rheobase current in *Setd5*$^{+/+}$ cells (without α-DTX, black, n =19; with α-DTX, blue, n =12), *Setd5*$^{+/-}$ cells (without α-DTX, red, n=21; with αDTX, purple, n = 13). **e**, Timeline of *in vivo* α-DTX cannula experiments. **f**, Confocal micrograph of a coronal section of the location of the cannula above the dPAG as well as the expression of neurobiotin that was infused into the cannula at the end of the experiments. Scale bar: 500 μm. **g**, Raster plots of mouse speed in response to the looming stimuli (white, dotted vertical lines denote the start of each loom; solid white line denotes the end of the stimulus) for *Setd5*$^{+/+}$ (upper, n = 6,

10 trials) and *Setd5*$^{+/-}$ (lower, n = 6, 15 trials), sorted by reaction time. **h**, as for **g** but for *Setd5*$^{+/+}$ (top, n = 6, 11 trials) and *Setd5*$^{+/-}$ (bottom, n = 6, 13 trials) animals after infusion of **α**-DTX (500nL, 500nM). **i**, Effect of **α**-DTX on reaction time. Before **α**-DTX (*Setd5*$^{+/+}$ versus *Setd5*$^{+/-}$; P = 0.017), effect of **α**-DTX on *Setd5*$^{+/+}$ (saline versus **α**-DTX; p = 0.104, paired *t*-test) and *Setd5*$^{+/-}$ (saline versus **α**-DTX; p = 0.014, paired *t*-test) and after **α**-DTX (*Setd5*$^{+/+}$ versus *Setd5*$^{+/-}$; P = 0.571). **j**, Effect of **α**-DTX on escape vigour. Before **α**-DTX (*Setd5*$^{+/+}$ versus *Setd5*$^{+/-}$; P = 0.052), effect of **α**-DTX on *Setd5*$^{+/+}$ (saline versus **α**-DTX; p = 0.760, paired *t*-test) and *Setd5*$^{+/-}$ (saline versus **α**-DTX; p = 0.649, paired *t*-test) and after **α**-DTX (*Setd5*$^{+/+}$ versus *Setd5*$^{+/-}$; P = 0.075). **k**, Shelter exit behaviour during the first LER trial when the mice are injected with saline (*Setd5*$^{+/+}$, black, top left; *Setd5*$^{+/-}$, red, bottom left) or **α**-DTX (*Setd5*$^{+/+}$, blue, top right; *Setd5*$^{+/-}$, purple, bottom right). Each row represents one animal, filled and open dots represent exits into the threat zone or not, respectively. **l**, Effect of **α**-DTX on shelter exits. Before **α**-DTX (*Setd5*$^{+/+}$ versus *Setd5*$^{+/-}$; P = 0.012), effect of **α**-DTX on *Setd5*$^{+/+}$ (saline versus **α**-DTX; p = 0.038, paired *t*-test) and *Setd5*$^{+/-}$ (saline versus **α**-DTX; p = 0.003, paired *t*-test) and after **α**-DTX (*Setd5*$^{+/+}$ versus *Setd5*$^{+/-}$; P = 0.495). Markers represent the average values across all trials for individual animals. Box-and-whisker plots show median, IQR and range. P-values: Wilcoxon's test, p-values: two-way repeated measures ANOVA, unless specified. For detailed statistics, see Supplementary Table 1.

Convergent behavioural deficits across ASD models.

To test whether the deficiencies observed are specific to *Setd5*$^{+/-}$ animals or might reveal a more general phenomenon across molecularly distinct ASD models, we decided to test two additional highly penetrant mutations, *Cullin3* (*Cul3*), a ubiquitin ligase-encoding gene, and *Ptchd1,* a member of the Patched family speculated to function as a Sonic hedgehog receptor. Similar to our previous experiments, we exposed *Cul3* and *Ptchd1* animals to the LER, resulting in qualitatively similar behavioural deficits (Fig. 6a,f). Both cohorts required, on average, more repetitions to elicit an escape response (Fig. 6b,g), had longer reaction times between the stimulus start and the maximum speed (Fig. 6c,h), and displayed slower vigour compared to their WT siblings (Fig. 6d,i). Similar to *Setd5*, these changes were not due to the animals not reacting to the first stimulus, as seen in their consistent arrest behaviour, nor to differences in adaptation, their location, head direction, or speed of the animal at stimulus onset (Extended Figs. 7, 8, Supplementary Figs. 2, 3). Similar to *Setd5*$^{+/-}$, the difference in response reaction time is an intrinsic and not an adaptive property since it is present during the first loom presentation (Extended Data Figs. 7h, 8e). However, they varied in strength, with *Cul3*$^{+/-}$ mice showing a less severe phenotype than the *Setd5*$^{+/-}$ or *Ptchd1*$^{Y/-}$ models. Interestingly, slower reaction times and reduced vigour could also be observed in *Ptchd*$^{Y/-}$ animals, despite their baseline hyperactivity (Supplementary Fig. 2a,f,g). Next, we tested if the deficiencies could be explained by changes in visual processing. Similar to our previous results (Fig. 2), we could not observe any visual deficits in either *Cul3*$^{+/-}$ nor *Ptchd1*$^{Y/-}$ (Extended Data Fig. 9). This result and the convergent nature of our behaviour across ASD models suggest that a dPAG hypoexcitability phenotype might be a widespread mechanism occurring beyond *Setd5*. To test this possibility, we recorded dPAG neurons in *Ptchd1* and *Cul3* animals. These experiments revealed that *Ptchd1* animals, despite having mostly identical intrinsic properties to their WT siblings (Extended Data Fig. 10ai-ii), also show a hypoexcitability phenotype at high current inputs (Fig. 6k,l). Contrary to *Setd5*, this phenotype was not rescued by **α**-DTX application, showing that similar physiological phenotypes can arise from distinct molecular mechanisms (Fig. 6k). In contrast to these physiological phenotypes, *Cul3* animals did not show any changes in neither their

current-firing relationship nor intrinsic properties (Fig. 6m,n, Extended Data Fig. 10aii-iii). These results indicate that despite the difference in the altered molecular pathways, models of autism can converge on similar behavioural deficits that are innate, quantifiable, and mediated by subcortical pathways.

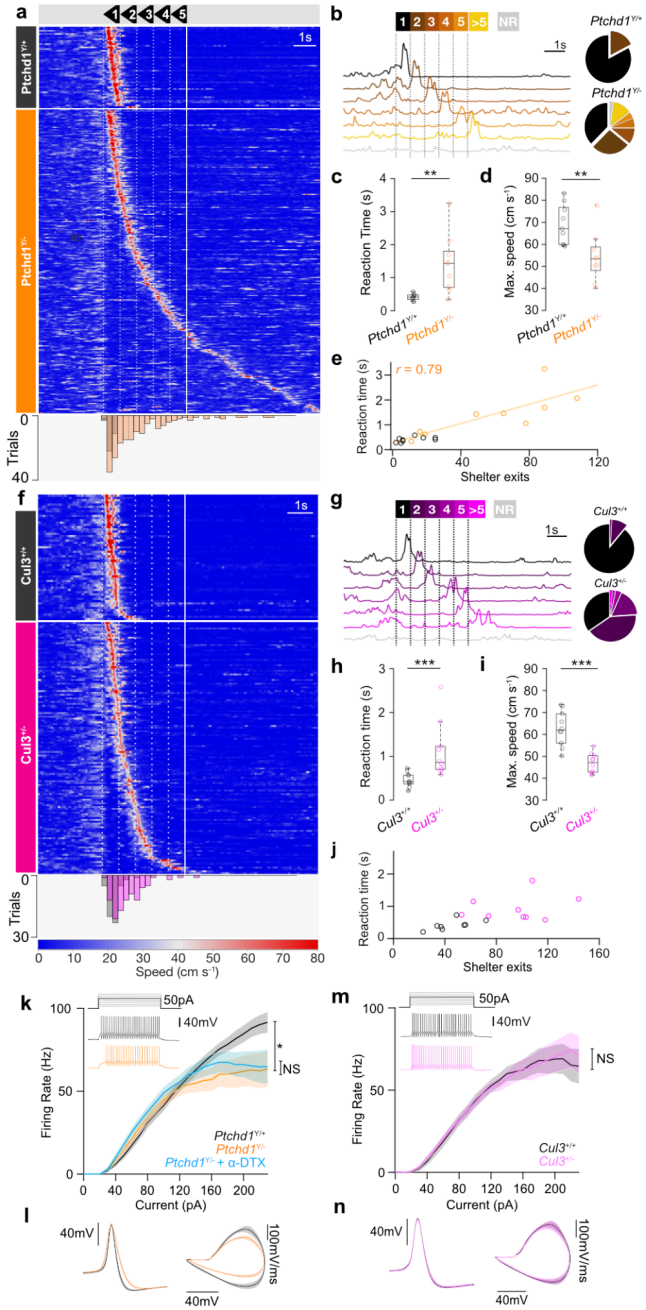

***Figure 6. Ptchd1* and *Cul3* models reveal distinct molecular and circuit mechanisms behind conserved decision-making delay. a**, Raster plot of mouse speed in response to looming stimuli (white, dotted vertical lines denote the start of each loom; white solid line denotes the end of the stimulus) for *Ptchd1*$^{Y/+}$ (top, n = 9, 49 trials) and *Ptchd1*$^{Y/-}$ (bottom, n = 9, 259 trials), sorted by reaction time. Bottom, distribution of reaction times for all *Ptchd1*$^{Y/+}$ (black) and *Ptchd1*$^{Y/-}$ (orange) trials, $p < 0.001$, two-way

Kolmogorov-smirnov (KS) test. **b**, Proportion of trials where the mice respond within 1 of the 5-loom stimuli, after the 5th or not at all (Right, *Ptchd1*$^{Y/+}$, top and *Ptchd1*$^{Y/-}$, bottom; Proportion of trials where mice escaped within the first loom: *Ptchd1*$^{Y/+}$, 0.826, *Ptchd1*$^{Y/-}$, 0.374, p = 0.004, two-way KS test.). Left, example traces from each category. **c**-**d**, Mean reaction time (**c**) and maximum escape speed (**d**) per animal, for all trials where the mice escaped (Reaction time; *Ptchd1*$^{Y/+}$, 0.411s, *Ptchd1*$^{Y/-}$, 1.41 s, P = 0.002. Maximum escape speed; *Ptchd1*$^{Y/+}$, 69.1 cms^{-1}, *Ptchd1*$^{Y/-}$, 54.2 cms^{-1}, *P* = 0.005). **e**, Relationship between the number of shelter exits and the average reaction time per animal (*Ptchd1*$^{Y/+}$, p = 0.126; *Ptchd1*$^{Y/-}$, *r* = 0.76, p = 0.012, Pearson's correlation). **f**, Raster plot of mouse speed in response to the looming stimuli (white, dotted vertical lines denote the start of each loom; solid white line denotes the end of the stimulus) for *Cul3*$^{+/+}$ top, n = 10, 61 trials) and *Cul3*$^{+/-}$ (bottom, n = 10, 112 trials), sorted by reaction time. Bottom, distribution of reaction times for all *Cul3*$^{+/+}$ (black) and *Cul3*$^{+/+}$ (pink) trials, p < 0.001, two-way KS test. **g**, Proportion of trials where the mice respond within 1 of the 5-loom stimuli, after the 5th or not at all (right, *Cul3*$^{+/+}$, top and *Cul3*$^{+/-}$, bottom; Proportion of trials where mice escaped within the first loom: *Cul3*$^{+/+}$, 0.892, *Cul3*$^{+/-}$, 0.347, p < 0.001, two-way KS test). Left, example traces from each category. **h**-**i**, Mean reaction time (**h**) and maximum escape speed (**i**) per animal, for all trials where the mice responded. (Reaction time; *Cul3*$^{+/+}$, 0.464 s, *Cul3*$^{+/-}$, 1.11 s, P < 0.001. Maximum escape speed; *Cul3*$^{+/+}$, 62.7 cm s^{-1}, *Cul3*$^{+/-}$, 46.8 cm s^{-1}, P < 0.001). **j**, Relationship between the number of shelter exits and the average reaction time per animal (*Cul3*$^{+/+}$, p = 0.078; *Cul3*$^{+/-}$, p = 0.571, Pearson's correlation). **k**, Summary of the relationship between current-injection and action potential firing showing a strong reduction in firing in *Ptchd1*$^{y/-}$ dPAG cells. Effect of genotype without α-DTX: p = 0.046; effect of α-DTX on *Ptchd1*$^{Y/-}$ firing: p = 0.680. (*Ptchd1*$^{Y/+}$, n = 4, 16 cells; *Ptchd1*$^{Y/-}$, n = 4, 20 cells; *Ptchd1*$^{Y/-}$ with α-DTX , n = 3, 13 cells). Inset, representative example traces to a 50 pA current injection for *Ptchd1*$^{Y/+}$ (black, top) and *Ptchd1*$^{Y/-}$ (orange, bottom). **l**, Average shape (left) and phase plane analysis (right) of the action potentials generated in the rheobase sweep (*Ptchd1*$^{Y/+}$, 16 cells, 58 spikes; *Ptchd1*$^{Y/-}$, 20 cells, 72 spikes). **m**, Summary of the relationship between current-injection and action potential firing in *Cul3* dPAG cells (*Cul3*$^{+/+}$, grey, 12 cells, n = 3; *Cul3*$^{+/-}$, pink, 12 cells, n = 3, p = 0.683 for the effect of genotype). **n**, Average shape (left) and phase plane analysis (right) of the action potentials generated in the rheobase sweep for *Cul3*$^{+/+}$ (grey, 68 spikes) and *Cul3*$^{+/-}$ (pink, 73 spikes). Box-and-whisker plots show median, IQR and range. Shaded areas represent SEM. Lines are shaded areas, mean ± s.e.m., respectively. P-values are Wilcoxon's test and p-values are two-way repeated measures ANOVA, unless specified. For detailed statistics, see Supplementary Table 1.

Discussion

Autism spectrum disorders (ASDs) are widespread in the global population, but our understanding of the disorder's origins remains limited. Advancements in genetic sequencing technologies have enabled the isolation of autism-risk genes, opening the door to several in-depth studies into the molecular mechanism of action of these genes[33]. However, there is a considerable mismatch between the observed wealth of molecular changes and our understanding of their roles in appropriate circuit function and, therefore, behaviour. Thus, direct comparisons across models have been difficult, leading to studies focusing on single models, defining particular changes but not general principles[34]. Here we show that the study of innate defensive behaviours provides a convergent behavioural framework that enables the directed analysis of the underlying sensorimotor processes up to the molecular level, permitting comparative dissections of the neuronal

dysfunctions across ASD models, an approach previously suggested for the understanding of complex systems[35,36].

Defensive escape behaviours are among the most basal perceptual decisions performed by animals[18]. Their finely-tuned mechanisms are indispensable for survival, but also for properly interacting with the environment. Whereas some stimuli unambiguously signal an imminent threat and should instruct immediate action, others are ambiguous and require adaptive responses arbitrated by the current context and state to decide, e.g., between ignoring, freezing, fighting, or escaping[18]. In mice, behavioural escape decisions are known to be initiated by the dPAG[24], where appropriate escape decisions are thought to be determined. While all tested ASD models can, in principle, respond behaviourally as robustly as their WT siblings, they require longer and respond with less vigour once an action has been initiated, hampering their ability to develop an appropriate fear memory to the threat zone (Figs. 1, 6, & Extended Data Figs. 1, 7, 8). The underlying changes were rigorously dissected in the *Setd5* haploinsufficient model, pointing to a specific misregulation of voltage-gated potassium channels in dPAG neurons that gives rise to a strong hypoexcitability phenotype (Figs. 3, 4, 5), namely Kv1.1, Kv1.2 or Kv1.6. Specifically, this indicates that the integration and action initiation required for adequate perceptual decision-making is disrupted in *Setd5* animals. These physiological phenotypes are tightly linked with behavioural deficiencies. Substantial threat evidence, either by strong optogenetic activation of dmSC neurons or high-contrast visual looms, elicit a slower and less robust response in *Setd5*$^{+/-}$ compared to their WT siblings. On the other hand, limited threat evidence, either by weak optogenetic activation or low-contrast looms, instructs similar behavioural responses between genotypes (Fig. 3). Accordingly, only strong current-injections that match the expected dPAG drive caused by high contrast loom[24] cause a Kv-channel induced hypoexcitability phenotype (Fig. 4d, 5), indicating that the delayed response phenotype is due to a dPAG dysfunction. This stimulus strength relationship aligns with the coping difficulties of many individuals with ASD to salient sensory stimuli, such as bright lights or crowded places, but not to mellow sensory environments[8].

The link between potassium channels and autism is well established. Genetic analyses of individuals with ASD uncovered deleterious mutations in potassium channels[37]. These, however, exclude Kv1.1. Interestingly, autistic-like repetitive and social behaviours in the *Scn2a* haploinsufficiency mouse model have been rescued in a Kv1.1 deficient background[38], supporting our results that enhancing and not disrupting Kv1.1's contribution through homeostatic misregulation can be a fundamental factor in ASD. Interestingly, the involvement of voltage-gated potassium channels in the generation of proper perceptual decisions appears to be a widespread principle across the animal kingdom, as recently shown in *Drosophila*[39].

The repetitive LER phenotype is associated with a reduction in fear memory to the threat zone and suggests that ASD mouse models are either less fearful or incapable of interpreting the noxiousness of threat experience appropriately (Fig. 1, Extended Data Figs. 1, 7, 8, Supplementary videos 1, 2), a maladaptive behaviour that recapitulates some human ASD traits[40]. Interestingly, this reduction of fear memory is directly linked with longer reaction times to the LER across ASD models (Fig. 1k,

Fig. 6 e, j), and thus, with the dPAG hypoexcitability phenotype (Fig. 4d). This correlation appears to be causally linked, given that the target-specific pharmacological rescue reverses both, the delayed PDM and fear memory to wild-type levels (Fig. 5e-l). Thus, maladaptive perceptual decisions, as with the delayed LER, can profoundly affect seemingly independent behavioural properties, emphasising the role of perception and subcortical pathways in ASD and learning in general.

As argued before[35], a careful experimental decomposition of behaviour is needed to examine its underlying processes and neuronal implementations. This argument can be further expanded for brain disorders, as done here, by defining a convergent behavioural phenotype across ASD models (Figs. 1, 6 & Extended Data Figs. 7, 8). While the mouse models studied here show deficiencies in PDM and fear memory, the underlying molecular deficits diverge. Whereas *Setd5* and *Ptchd1* dPAG neurons show a hypoexcitability phenotype (Figs. 4d-f, 6k,l & Extended Data Figs. 5,6), the weaker LER deficits in *Cul3* are independent of dPAG intrinsic properties (Fig. 6m,n). These results align with a previous characterisation that demonstrated that thalamic reticular impairments in *Ptchd1* animals are linked to a reduction in the conductance of calcium-dependent potassium currents[23] compared to deficits in cytoskeleton protein homeostasis and cell migration abnormalities in *Cul3* animals[22]. Thus, by providing a common behavioural criterion, we have established a platform to test the causality of changes in neuronal implementation, reflective of the described molecular complexity of ASD.

The diagnostic criteria for autism are behavioural and are mainly focused on abnormal social interactions, communication deficits, and repetitive behaviours. Thus, in animal models, a strong focus has been devoted to generating a comprehensive set of assays to study these abnormal behaviours as tools for discovering effective treatments[41]. Sensory processing and perceptual abnormalities have been shown to co-occur with classical ASD diagnostic criteria and have been recently proposed as promising behavioural biomarkers of autism[3]. However, as with the classical behavioural paradigms, perceptual tasks are mediated by complex neural circuits and are often difficult to evaluate and interpret experimentally. Here, we have shown that an innate perceptual decision-making (PDM) paradigm - the looming escape response (LER) - provides a quantitative framework to systematically link behavioural metrics with the relevant molecular changes, and thus, may reveal therapeutic targets as envisioned by precision medicine approaches in autism[33]. These primitive perceptual pathways are embedded in key behavioural nodes, such as the PAG[42], that can affect seemingly unrelated behaviours, e.g., LER, threat-induced fear memory and the emergence of repetitive behaviours (Suppl. Videos 1 & 2). Our work links innate PDM dysfunctions with ASD. Future studies designed to dissect the causal relationships between PDM and social and communication difficulties will be a revealing avenue to build a comprehensive view of ASD.

References

1. Baron-Cohen, S., Leslie, A. M. & Frith, U. Does the autistic child have a 'theory of mind' ? *Cognition* **21**, 37–46 (1985).
2. Tomchek, S. D. & Dunn, W. Sensory processing in children with and without autism: a comparative study using the short sensory profile. *Am. J. Occup. Ther.* **61**, 190–200 (2007).
3. Robertson, C. E. & Baron-Cohen, S. Sensory perception in autism. *Nat. Rev. Neurosci.* **18**, 671–684 (2017).
4. Pelphrey, K. A., Shultz, S., Hudac, C. M. & Vander Wyk, B. C. Research review: Constraining heterogeneity: the social brain and its development in autism spectrum disorder. *J. Child Psychol. Psychiatry* **52**, 631–644 (2011).
5. Buckner, R. L., Andrews-Hanna, J. R. & Schacter, D. L. The brain's default network: anatomy, function, and relevance to disease. *Ann. N. Y. Acad. Sci.* **1124**, 1–38 (2008).
6. Minshew, N. J. & Williams, D. L. The new neurobiology of autism: cortex, connectivity, and neuronal organization. *Arch. Neurol.* **64**, 945–950 (2007).
7. Simmons, D. R. *et al.* Vision in autism spectrum disorders. *Vision Res.* **49**, 2705–2739 (2009).
8. McFadyen, J., Dolan, R. J. & Garrido, M. I. The influence of subcortical shortcuts on disordered sensory and cognitive processing. *Nat. Rev. Neurosci.* **21**, 264–276 (2020).
9. Kleinhans, N. M. *et al.* fMRI evidence of neural abnormalities in the subcortical face processing system in ASD. *Neuroimage* **54**, 697–704 (2011).
10. Hadjikhani, N. *et al.* Look me in the eyes: constraining gaze in the eye-region provokes abnormally high subcortical activation in autism. *Sci. Rep.* **7**, 3163 (2017).
11. Hu, Y. *et al.* A translational study on looming-evoked defensive response and the underlying subcortical pathway in autism. *Sci. Rep.* **7**, 14755 (2017).
12. Jones, W. & Klin, A. Attention to eyes is present but in decline in 2–6-month-old infants later diagnosed with autism. *Nature* vol. 504 427–431 Preprint at https://doi.org/10.1038/nature12715 (2013).

13. Volkmar, F. R., Lord, C., Bailey, A., Schultz, R. T. & Klin, A. Autism and pervasive developmental disorders. *J. Child Psychol. Psychiatry* **45**, 135–170 (2004).

14. Madipakkam, A. R., Rothkirch, M., Dziobek, I. & Sterzer, P. Unconscious avoidance of eye contact in autism spectrum disorder. *Sci. Rep.* **7**, 13378 (2017).

15. Tokuoka, K., Kasai, M., Kobayashi, K. & Isa, T. Anatomical and electrophysiological analysis of cholinergic inputs from the parabigeminal nucleus to the superficial superior colliculus. *J. Neurophysiol.* **124**, 1968–1985 (2020).

16. Jure, R. Autism Pathogenesis: The Superior Colliculus. *Front. Neurosci.* **12**, 1029 (2018).

17. Yilmaz, M. & Meister, M. Rapid innate defensive responses of mice to looming visual stimuli. *Curr. Biol.* **23**, 2011–2015 (2013).

18. Branco, T. & Redgrave, P. The Neural Basis of Escape Behavior in Vertebrates. *Annu. Rev. Neurosci.* **43**, 417–439 (2020).

19. Deliu, E. *et al.* Haploinsufficiency of the intellectual disability gene SETD5 disturbs developmental gene expression and cognition. *Nat. Neurosci.* **21**, 1717–1727 (2018).

20. Bandler, R., Depaulis, A. & Vergnes, M. Identification of midbrain neurones mediating defensive behaviour in the rat by microinjections of excitatory amino acids. *Behav. Brain Res.* **15**, 107–119 (1985).

21. Deng, H., Xiao, X. & Wang, Z. Periaqueductal Gray Neuronal Activities Underlie Different Aspects of Defensive Behaviors. *J. Neurosci.* **36**, 7580–7588 (2016).

22. Morandell, J. *et al.* Cul3 regulates cytoskeleton protein homeostasis and cell migration during a critical window of brain development. *Nat. Commun.* **12**, 1–22 (2021).

23. Wells, M. F., Wimmer, R. D., Schmitt, L. I., Feng, G. & Halassa, M. M. Thalamic reticular impairment underlies attention deficit in Ptchd1Y/− mice. *Nature* **532**, 58–63 (2016).

24. Evans, D. A. *et al.* A synaptic threshold mechanism for computing escape decisions. *Nature* **558**, 590–594 (2018).

25. Zhao, X., Liu, M. & Cang, J. Visual cortex modulates the magnitude but not the selectivity of

looming-evoked responses in the superior colliculus of awake mice. *Neuron* **84**, 202–213 (2014).

26. Pavón Arocas, O. Biophysical properties and gene expression profile of single periaqueductal gray neurons. (UCL (University College London), 2022).
27. Zbili, M. *et al.* Homeostatic regulation of axonal Kv1.1 channels accounts for both synaptic and intrinsic modifications in the hippocampal CA3 circuit. *Proc. Natl. Acad. Sci. U. S. A.* **118**, (2021).
28. Morgan, P. J., Bourboulou, R., Filippi, C., Koenig-Gambini, J. & Epsztein, J. Kv1.1 contributes to a rapid homeostatic plasticity of intrinsic excitability in CA1 pyramidal neurons in vivo. *Elife* **8**, (2019).
29. Grubb, M. S. & Burrone, J. Activity-dependent relocation of the axon initial segment fine-tunes neuronal excitability. *Nature* **465**, 1070–1074 (2010).
30. Winklhofer, M. *et al.* Analysis of phosphorylation-dependent modulation of Kv1.1 potassium channels. *Neuropharmacology* **44**, 829–842 (2003).
31. Niespodziany, I. *et al.* Discovery of a small molecule modulator of the Kv1.1/Kvβ1 channel complex that reduces neuronal excitability and in vitro epileptiform activity. *CNS Neurosci. Ther.* **25**, 442–451 (2019).
32. Wei, P. *et al.* Processing of visually evoked innate fear by a non-canonical thalamic pathway. *Nat. Commun.* **6**, 6756 (2015).
33. Kostic, A. & Buxbaum, J. D. The promise of precision medicine in autism. *Neuron* **109**, 2212–2215 (2021).
34. Willsey, H. R., Willsey, A. J., Wang, B. & State, M. W. Genomics, convergent neuroscience and progress in understanding autism spectrum disorder. *Nat. Rev. Neurosci.* **23**, 323–341 (2022).
35. Krakauer, J. W., Ghazanfar, A. A., Gomez-Marin, A., MacIver, M. A. & Poeppel, D. Neuroscience needs behavior: Correcting a reductionist bias. *Neuron* **93**, 480–490 (2017).
36. Marr, D. *Vision*. (MIT Press, 2010).
37. Guglielmi, L. *et al.* Update on the implication of potassium channels in autism: K+ channelautism spectrum disorder. *Front. Cell. Neurosci.* **9**, (2015).
38. Indumathy, J., Pruitt, A., Gautier, N. M., Crane, K. & Glasscock, E. Kv1.1 deficiency alters repetitive

and social behaviors in mice and rescues autistic-like behaviors due to Scn2a haploinsufficiency. *Brain Behav.* **11**, e02041 (2021).

39. Groschner, L. N., Chan Wah Hak, L., Bogacz, R., DasGupta, S. & Miesenböck, G. Dendritic Integration of Sensory Evidence in Perceptual Decision-Making. *Cell* **173**, 894–905.e13 (2018).
40. Macari, S. *et al.* Emotional Expressivity in Toddlers With Autism Spectrum Disorder. *J. Am. Acad. Child Adolesc. Psychiatry* **57**, 828–836.e2 (2018).
41. Silverman, J. L., Yang, M., Lord, C. & Crawley, J. N. Behavioural phenotyping assays for mouse models of autism. *Nat. Rev. Neurosci.* **11**, 490–502 (2010).
42. Behbehani, M. M. Functional characteristics of the midbrain periaqueductal gray. *Prog. Neurobiol.* **46**, 575–605 (1995).
43. Yang, H., Wang, H. & Jaenisch, R. Generating genetically modified mice using CRISPR/Cas-mediated genome engineering. *Nat. Protoc.* **9**, 1956–1968 (2014).
44. Brainard, D. H. The Psychophysics Toolbox. *Spat. Vis.* **10**, 433–436 (1997).
45. Gupta, D., Młynarski, W., Symonova, O., Svatoň, J. & Joesch, M. Panoramic visual statistics shape retina-wide organization of receptive fields. *bioRxiv* 2022.01.11.475815 (2022) doi:10.1101/2022.01.11.475815.
46. Pachitariu, Steinmetz & Kadir. Fast and accurate spike sorting of high-channel count probes with KiloSort. *Adv. Neural Inf. Process. Syst.*
47. Lee, K. H., Tran, A., Turan, Z. & Meister, M. The sifting of visual information in the superior colliculus. *Elife* **9**, (2020).
48. Stitt, I., Galindo-Leon, E., Pieper, F., Engler, G. & Engel, A. K. Laminar profile of visual response properties in ferret superior colliculus. *J. Neurophysiol.* **110**, 1333–1345 (2013).
49. Montijn, J. S. *et al.* ZETA: a parameter-free statistical test for neuronal responsiveness. *bioRxiv* 2020.09.24.311118 (2021) doi:10.1101/2020.09.24.311118.
50. Mathis, A. *et al.* DeepLabCut: markerless pose estimation of user-defined body parts with deep learning. *Nat. Neurosci.* **21**, 1281–1289 (2018).

Acknowledgments

We thank Prof. Peter Jonas for his suggestion on the involvement of potassium channels and members of the Neuroethology group for their comments on the manuscript. Katalin Szigeti and Julie Murmann for experimental help. This research was supported by the Scientific Service Units of IST Austria through resources provided by the Lab Support Facility, the Imaging and Optics Facility, the Machine Shop Unit and the Preclinical Facility, especially Freyja Langer and Michael Schunn. This work was supported by a European Research Council Starting Grant 756502 (MJ).

Author contributions

LB and MJ designed the study. LB analysed all data with help from OS. LB performed the behavioural, optogenetic, α-DTX cannula, and *in vivo* electrophysiology experiments with help from TVZ. PK performed the *in vitro* experiments. LB, MJ and OS developed the behavioural system and analysis pipeline. TVZ, OS and MJ developed the *in vivo* electrophysiology setup and LB the analysis pipeline. TM performed the protein level analysis. XC, GN and TR generated the *Ptchd1* mouse line. GN and RS provided mouse lines, reagents and gave advice on the study design. LB and MJ wrote the manuscript with help of the other authors.

Competing interests

Authors declare that they have no competing interests.

Methods

Mice

The study was discussed and approved by the institutional ethics committee of the University of Veterinary Medicine Vienna and the Institute of Science and Technology Austria in accordance with good scientific practice guidelines and national legislation under license numbers BMWF-68.205/0023-II/3b/2014 and 66.018/0017-WF/V/3b/2017. Male and female adult *Setd5*$^{+/-}$, *Setd5*$^{+/fl}$::*Emx1*-Cre, *Setd5*$^{+/-}$::*VGluT2*-ires-Cre, *Cul3*$^{+/-}$, *Ptchd1*$^{Y/-}$ mice were housed under a 12h light/dark cycle (lights on at 07:00), with food and water available *ad libitum*. The animals were housed in groups of 2-6 animals per cage and were tested during the light phase. Animals used for the *in vivo* electrophysiological recordings or freely-moving optogenetics experiments were group housed before surgery and individually housed after the surgery. Mice were chosen based on genotypes. Sex-matched animal pairs of control-mutant siblings from the same litters were compared to decrease variance due to age, environment and genetic background. For the number and sex of animals used in the experiments, please refer to Supplementary Table 1.

METHOD DETAILS

Generation of Ptchd1$^{Y/-}$ mice

Ptchd1$^{Y/-}$ mice for analysis were generated using the CRISPR/Cas9 system, as described in [43]. In brief, *in vitro* transcribed sgRNAs targeting the exon 2 of *Ptchd1* were microinjected into zygotes of C57BL/6NRj mice together with Cas9 *mRNA*. Offspring were screened by PCR for deletions using primers spanning the target sites (5′-GTAGGGCTGGAATCATGAGG-3′, 5′-CACATCCTTTGGTGTGATGC-3′). Deletion of *Ptchd1* exon 2 was confirmed by Sanger sequencing analyses. The founder line was established from a female *Ptchd1*$^{+/-}$ mouse with a 1.26 kb deletion. Analysis of *Ptchd1* transcript level by RT-PCR confirmed impaired *Ptchd1* expression in brain, cerebellum and kidney of the *Ptchd1*$^{Y/-}$ mice, compared to control mice.

Behavioural procedures

Experimental setup. All behavioural experiments were performed at mesopic light levels, in a square, black, IR-transparent Perspex box (W: 32 cm x L: 32 cm x H: 32 cm) with a shelter made of the same material (9 cm x 9 cm x 3 cm) positioned in one corner. One wall of the box was 2 cm shorter to allow for ventilation and for the optic fibre to pass through for optogenetic experiments. A plastic screen covered with a plastic sheet with a matte surface was placed as a lid on top of the box, and a modified Texas Instruments DLP projector (DLP CR4500EVM) back-projected a grey background. The blue LED was exchanged for a high-power UV-LED (ProLight 1W UV LED, peak 405 nm) to improve the differential stimulation of S pigments. The experiments were recorded with a near-IR camera (acA1920-150um, Basler, 60 Hz) from below the centre of the arena. Video recording, visual and optogenetic stimulation were controlled using custom software written in MATLAB, python and Arduino. The entire apparatus was housed within a sound-deadening,

light-proof cabinet which was illuminated by an infrared light-emitting diode (LED) lamp (SIL 616.21, Sanitas).

Protocols. All animals were habituated to the test arena at least one day before testing and were allowed to explore the arena for at least 20 mins. The initial 10 min of this exploration time was recorded and used to analyse the animals' exploratory behaviour (Supplementary Fig. 1). For the looming escape response (LER: Figs. 1 & Extended Data Figs. 1, 2, 3, 8, 9) paradigm, responses were tested over five consecutive days. On each test day the animals were given 10 min to acclimatise to the arena, after which they were subjected to 3 test trials, with a 3 min interval between each trial. Each trial lasted 180 s, within which the central position of the mouse was tracked online (Python) and was used to trigger the visual stimuli in a closed-loop manner whenever the mouse crossed a designated threshold distance (10 cm) from the centre of the shelter, with a minimum stimulus interval of 30 s. A typical experiment lasted ~30 min and the entire arena was cleaned with 70 % ethanol between animals.

In preparation for the reward trials, after the 4th day of testing a small piece of banana chip was placed in the opposite corner of the arena to the shelter and the mice were free to explore the arena without triggering any loom stimuli. The animals were left to explore until they successfully acquired the banana chip, after which time both the mouse and the chip were placed back in their home cage. The reward trial then took place after the 5th day of testing. Another small piece of banana chip was again placed in the opposite corner of the arena and the animals were free to explore, however this time whenever the mouse passed the threshold distance from the shelter a looming stimulus would start, this time with no inter-stimulus interval. For different contrast experiments, animals were presented with looming stimuli of 20, 50 or 98 % contrast in a pseudorandom order upon crossing the trigger threshold. The background luminosity remained constant while the luminance of the disc was increased to generate low contrast stimuli.

Visual Stimuli. Stimuli were created and presented using custom-made scripts in MATLAB (MathWorks, Inc.), using the Psychophysics Toolbox extensions[44]. The standard stimulus consisted of a dark disc on a grey background presented on the lid over the centre of the arena, that reached a maximum size of 40 deg/visual angle. The disc expanded over 500 ms at a speed of 80 deg s^{-1} and then remained at this size for 250 ms before disappearing and a new expanding disc immediately appearing. A maximum of 5 expanding discs were shown in a single loom bout. A red rectangle was presented along one side of the projected image every 5th frame, onto an out-of-view section of the arena lid. An optical filter reflected this red light back towards a photodiode (PDA36A2, ThorLabs) and this information was then used for post-hoc synchronisation of the behavioural data and the stimulus.

Viruses

The viruses used in this study: for optogenetic activation, adeno-associated virus (AAV) AAV9-EF1a-DIO-hChR2(E123T)T159C)-EYFP-WPRE-hGH (1×10^{13} viral genomes per ml (vg ml^{-1}),

Addgene 35509); for control experiments, AAV9-Syn-Flex-GCaMP6m-WPRE-SV40 (1×10^{13} vg/ml, Addgene 100838).

Surgical procedures

Mice were anaesthetised with an intraperitoneal (i.p.) injection of ketamine (95 mg kg^{-1}) and xylazine (4.5 mg kg^{-1}), followed by metamizol (20 mg kg^{-1}, i.p.) and buprenorphine (0.05 mg kg^{-1}, i.p.) and meloxicam (2 mg kg^{-1}, subcutaneous (s.c.)). If needed, isoflurane (0.5-2 % in oxygen, 0.8 l min^{-1}) was used to maintain anaesthesia. Fur on the top of the head was removed with an electric hair remover (Braun Precision Trimmer, PT 5010) then the mice were placed in a stereotaxic frame (Model 962, Kopf Instruments) and fixed using the ear bars. Eyes were protected using Oleo Vital eye cream and a topical analgesic (Xylocain 2 % gel) was applied to the skin with a q-tip before cutting the skin. Craniotomies of were made using 0.5 mm burrs (Fine Science Tools) and dental drill (Foredom, HP4-917) and viral vectors were delivered using pulled pipettes (World Precision Instruments, 1.4 mm OD, 0.53 mm ID, #504949) made with a micropipette puller (DMZ Zeitz-puller, Germany) and delivered using an automatic nanoinjector (World Precision Instruments, Nanoliter 2010) at 20 nl min^{-1}. The skin was closed after surgery using surgical glue (Vetbond, 3M, #1469SB).

Optogenetics experiments

Surgical procedure. Setd5$^{+/+}$::VGluT2-ires-Cre and Setd5$^{+/-}$::VGluT2-ires-Cre sex-matched sibling mice were injected with AAV9-DIO-ChR2-eYFP (see Viruses) into the right dmSC (75-100 nl, ML: -0.5, AP: -0.5 to -0.7, DV: -1.45 to -1.6, from lambda). Control mice were injected with 100nl of AAV9-Flex-GCaMP6m into the right dmSC at the same coordinates. One optic fibre (400 µm diameter, CFMC54L02, ThorLabs) was implanted 250 µm dorsal to the injection site. Fibres were affixed using light-curing glue (Optibond Universal, Kerr Dental) and dental cement (SuperBond C&B Kit, Hentschel-Dental) and the skin was closed around the implant with surgical glue (Vetbond, 3M, #1469SB).

Experimental paradigm. The same behavioural arena was used for the optogenetic activation experiments except with the addition of a black piece of perspex (9 cm x 5 cm) positioned 10 cm above the floor in place of the closed shelter. Mice were similarly acclimatised to the arena, as in the LER procedure, but with the fibre optic cable (200 µm, 0.48 NA, Doric Lenses) attached via a rotary joint (RJ1, ThorLabs) to allow for unrestrained movement and minimal handling of the animals. Since it has previously been shown[24] that increasing light intensity can be used as a proxy for the level of mSC, and hence dPAG, activation we decided to systematically modulate the laser light intensity in different trials. Once the trial began, mice were photostimulated (473 nm, 10 light pulses of 10 ms at 10 Hz; Shanghai Dream Lasers Technology) if they passed the threshold distance (10 cm) from the shelter, with a minimum inter-stimulus interval of 30 s. The initial laser intensity was set to a low irradiance (0.01-0.1 mW mm^{-2}) that did not evoke an observable behavioural response, however after at least 3 trials (180 s each, with a maximum 5 triggers per trial) at each intensity the irradiance was increased by (0.25-0.5 mW mm^{-2}). Laser power never exceeded 12 mW mm^{-2}. Two mice never elicited an observable escape behaviour, and

post-processing histological analysis revealed mislocalised viral expression in these animals, and they were excluded from the analysis, along with their matched siblings.

In vivo electrophysiology

Data acquisition. A 32-channel silicon probe (NeuroNexus, USA, A32-OM32) was used to record extracellular spikes from different depths of the SC in *Setd5*$^{+/+}$ (n = 3), *Setd5*$^{+/-}$ (n = 3), *Cul3*$^{+/+}$ (n = 3), *Cul3*$^{+/-}$ (n = 3), *Ptchd1*$^{Y/+}$ (n = 3) and *Ptchd1*$^{Y/-}$ (n = 3) sex-matched sibling mice. Mice were implanted with a custom-designed head plate over a ~0.5-1 mm diameter craniotomy (left hemisphere, AP: 0.4 to -0.4, ML: 0.4 to 0.8 from lambda) and a second craniotomy (~0.5 mm) was made anterior to bregma on the right hemisphere, where a reference gold pin was implanted and lowered until it touched the brain surface. Both were cemented to the skull using light-curing glue (Optibond Universal, Kerr Dental) and dental cement (SuperBond C&B Kit, Hentschel-Dental), with the headplate additionally fixed using Charisma Flow (Kulzer GmBH). The craniotomy was covered with Kwik-Cast (World Precision Instruments) to protect the underlying tissue before recording. At least 24 hrs after surgery, mice were placed on a suspended spherical treadmill (20 cm diameter) and head-fixed within a toroidal screen covering 190 ° of visual angle which was illuminated by a DLP-light projector (Blue LED exchanged for UV 405 nm, 60 Hz) reflecting off a spherical mirror in front of the screen (see diagram in Fig. 2a). The behaviour of the animal was recorded by a near-IR camera (Basler, acA1920-150um, 30 Hz) from the reflection of the animal in an IR-reflective heat mirror positioned 30 cm from the face of the mouse and 35 cm from the camera. Prior to recording, the probe was coated with DiI (1 mM in ethanol, Merck, #42364) for later histological confirmation of the recording site and a wire was connected to the ground pin for both an external reference and ground. The kwik-cast seal was removed, revealing the brain surface and the confluence of the overlying superior sagittal and the left transverse sinus. Care was taken to position the probe as posteriorly and as medially as possible without damaging the sinuses or other blood vessels. It was then lowered, zeroed at the brain surface then slowly lowered into the overlying cortex and the SC at 1 mm s^{-1} to depths between 1.2-2.2 mm. The recording was started 15 min after reaching the desired depth to allow for stabilisation. The probe was lowered to 3-4 depths per animal with 250 µm intervals, to sample from cells across the depth of the SC. Each recording took ~30 min, with the animal in the setup for ~180 min in total. Data was recorded at 20 kHz (PCIe-6321, National instruments and Intan board RHD2000 Evaluation Board version 1.0).

Visual Stimuli (*in vivo* electrophysiology)

Sensory stimuli were made using the Psychophysics Toolbox extensions in MATLAB (MathWorks, Inc.) and presented and synchronised using custom-made LabVIEW software. Frames were presented at a refresh rate of 60 Hz. At each depth, the mice were exposed to one 20 min presentation of a full field shifting spatiotemporal white-noise stimulus (see [45]) in order to assess receptive fields, and two repetitions of the remaining stimuli (5 x loom bouts, moving bars, moving gratings, full field flash). Each presentation would start with a uniform grey screen (60 s, green and UV LED intensities were set to match the sun spectrum from a mouse opsin perspective), followed by the first presentation of the looming stimulus, then the other stimuli in a pseudorandom order

separated by 30 s gaps of a grey screen. White-noise "checker" stimuli were presented at 20 Hz update for 10 min. The checker size was 6.56 deg^2 and the entire grid was shifted between 0 and 3.25 deg in both x- and y-axis after every frame. Auditory monitoring of responses to a flashing point stimulus was used in real-time to gauge the rough centre of the receptive fields of the neurons being recorded and the location of the looming stimulus was positioned to overlap with this position. The looming stimulus consisted of 10 repetitions of 5 sequential, individual looming stimuli (a loom bout), as previously described in the behavioural experiments. These loom bouts would be presented with intervals of pseudorandom lengths between 10-30 s with a grey screen in between. To assess direction selectivity, the mice were presented with full-filed moving square gratings (1.5 cycles s^{-1} temporal frequency and 0.3 cycles deg^{-1} spatial frequency) or a wide dark bar (38 deg s^{-1} speed, 6.5 deg width) in four orientations, drifting in eight different directions (separated by 45 deg) repeated twice for each orientation. Full field ON-OFF flashes were presented in blocks of 10 repetitions of 0.5 s OFF, 1 s ON and 0.5 s OFF stimuli.

***In vitro* electrophysiology**

Mice were deeply anesthetised via intraperitoneal (i.p.) injection of ketamine (95 mg kg^{-1}) and xylazine (4.5 mg kg^{-1}), followed by transcardial perfusion with ice-cold, oxygenated (95 % O_2, 5 % CO_2) artificial cerebrospinal fluid (ACSF) containing (in mM): 118 NaCl, 2.5 KCl, 1.25 NaH_2PO_4, 1.5 $MgSO_4$, 1 $CaCl_2$, 10 Glucose, 3 Myo-inositol, 30 Sucrose, 30 $NaHCO_3$; pH = 7.4. The brain was rapidly excised and coronal sections of 300 µm thickness containing the SC and PAG were cut using a Linear-Pro7 vibratome (Dosaka, Japan). Slices were left to recover for 20 min at 35°C, followed by a slow cool down to room temperature (RT) over 40 – 60 min. After recovery, one slice was transferred to the recording chamber (RC-26GLP, Warner Instruments, Holliston, MA, USA) and superfused with ACSF containing 2 mM $CaCl_2$ and 20 µM bicuculline methiodide (Tocris) at a rate of 3 – 4 ml/min at RT. In experiments using 100 nM α-dendrotoxin (Alomone Labs, Jerusalem, Israel), 0.1 % bovine serum albumin (BSA) was added to the ACSF. Glass pipettes (B150-86-10, Sutter Instrument, Novato, CA, USA) with resistances of 3 – 4 MΩ were crafted using a P1000 horizontal pipette puller (Sutter Instrument) and filled with internal solution containing (in mM): 130 K-Gluconate, 10 KCl, 5 $MgCl_2$, 5 MgATP, 0.2 NaGTP, 0.5 EGTA, 5 HEPES; pH 7.4 adjusted with KOH. Biocytin (0.2 – 0.3 %) was added to the internal solution for post hoc morphological reconstruction. Neurons of the dPAG or the dmSC were visually identified using an infrared differential interference contrast video system in a BX51 microscope (Olympus, Tokyo, Japan). Electrical signals were acquired at 20 – 50 kHz and filtered at 4 kHz using a Multiclamp 700B amplifier (Molecular Devices, San Jose, CA, USA) connected to a Digidata 1440A digitizer (Molecular Devices) with pClamp10 software (Molecular Devices). Spontaneous excitatory postsynaptic currents (sEPSCs) were recorded at –60 mV for at least 1 min. Intrinsic membrane properties and neuronal excitability were measured in current clamp mode by applying current steps from –20 to 200 pA for 1 s in 10 pA increments. Access resistance was constantly monitored between protocols and recordings with access resistances exceeding 20 MΩ or with changes in access resistance or holding current by more than 20 % were discarded. After recordings, the

pipette was carefully withdrawn and the slice was transferred to 4 % paraformaldehyde (PFA) in PBS solution.

In vivo cannula experiments

Surgical procedure. Setd5$^{+/+}$ and Setd5$^{+/-}$ sex-matched sibling mice were implanted with a single infusion cannula (C315IS-5/SPC, 33GA, 5mm) above the dorsal PAG (ML: -0.5, AP: -0.8 to -1, DV: -1.5 to -1.65, from lambda). Fibres were affixed using light-curing glue (Optibond Universal, Kerr Dental) and dental cement (SuperBond C&B Kit, Hentschel-Dental) and the skin was closed around the implant with surgical glue (Vetbond, 3M, #1469SB).

Experimental paradigm. The same behavioural arena was used for the cannula experiments with α-dendrotoxin (α-DTX). Two weeks after mice were implanted with the cannula they were acclimatised to the arena for 20 minutes and gently handled. 48 hours after acclimatisation to the arena, the mice were attached to the infusion system (tubing (PlasticsOne C313CT), infusion cannula (C315IS-5/SPC, 33GA, 5mm), guide cannula (PlasticsOne, C315GS-5/SF, 26GA, 5mm) and a 0.5 µL manual syringe (Model 7000.5, #86250, Hamilton) and placed into an open cage to allow them to move freely during the infusion of 500nL of saline with 0.1 % bovine serum albumin (BSA) at 100nl min^{-1}. The mice were left for a further 5 min before detaching them from the infusion system and placing them within the arena. The mice were recorded for 5 minutes when they were first placed in the arena, then 15 minutes after the start of infusion, one trial of the standard LER trial was initiated. 48 hours after the first LER trial with saline, the mice were reattached to the infusion system and α-DTX (500nL, 500nM in 0.1 % BSA) was infused at 100nl min^{-1}. The mice were again left for 5 minutes before being detached and placed into the arena. 15 minutes after the start of the infusion the standard LER trial was initiated. This time, there was a 3 min gap between LER trials and 3 trials were conducted, as in the standard LER test. After the last test, the mice were re-attached to the infusion system and infused with 500nL of a 10% solution of neurobiotin in sterile saline at 100nl min^{-1}, left for 5 minutes, then detached and placed back into their home cages. The animals were sacrificed 48 hours after infusion with neurobiotin and later stained with Streptavidin-594.

Histology

For fluorescent immunostainings and histological confirmation of fibre and probe locations, adult *Setd5*$^{+/+}$ and *Setd5*$^{+/-}$ mice were transcardially perfused with 4 % paraformaldehyde (PFA) and their brains were dissected, post-fixed overnight in 4 % PFA, washed with 1X PBS, dehydrated in a 30 % sucrose solution and sectioned with a freezing microtome (SM2010R, Leica) to 100 µm (for probe/fibre/cannula confirmation) and 40 µm (for immunostainings) thick slices. For histological confirmation of probe and fibre locations, the sections were rinsed in PBS, stained with 4',6-diamidino-2-phenylindole (DAPI; 2 mM in PBS) and mounted on Superfrost glass slides in a mounting medium containing 1,4-diazabicyclooctane (DABCO; Sigma, D27802) and Mowiol 4-88 (Sigma, 81381). For Kv1.1 immunostainings, tissue was rinsed and then blocked for 1 hour at room temperature in a buffer solution containing 10% normal donkey serum (Abcam, ab7475), 0.1 %

Triton X-100 in PBS. Primary antibodies (Kv1.1, Rabbit, 1:200; Rb-Af400, Frontier Institute) were diluted in a blocking buffer and incubated for 48 hours at 4 °C. The tissue was then rinsed 3 times in PBS and left overnight to wash at 4 °C. Secondary antibodies (Alexa-594 Donkey anti-rabbit, 1:1000; R37119, Thermo Fisher) were diluted in 1X PBS and incubated for 2 hrs at room temperature in the dark, before being washed three more times in 1X PBS before being counter-stained with DAPI and mounted as for histological sections described above. Sections were imaged with either a confocal microscope (LSM800, Zeiss), at 63X or 20X magnification, or a wide-field microscope (VS120, Olympus), at 10X magnification.

For visualisation of the dPAG/dmSC cells recorded *in vitro* and the neurobiotin infused into the cannula implanted mice, tissue sections were washed in 1X PBS for 10 minutes then a solution of Streptavidin (1:100, 1 mg/ml, Thermo Fisher Scientific, S11227) in PBS with 0.3% Triton-X was added and the samples were left at 4 °C overnight. The tissue was then washed three times with PBS, *in vitro* slices were mounted into a custom designed chamber for thick slices and imaged with a confocal microscope (LSM800, Zeiss) at 20X (90 µm projection, 2 µm sections) and 40X (50 µm projection, 1 µm sections).

Western blot

Tissue samples from the superior colliculus, periaqueductal grey (PAG) and cortex were dissected from *Setd5*$^{+/+}$ (n = 3) and *Setd5*$^{+/-}$ (n = 3) mice. PAG tissue was dissected using a 2 mm diameter biopsy punch (ID: 2 mm, OD: 3 mm, Fine Science Tools, 18035-02). Each purification was performed independently three times and samples were stored at -80 °C until further processing. Samples were Dounce homogenized 15 times with 300 mL RIPA buffer (50 mM Tris-HCl, 150 mM NaCl, 0.5 % sodium deoxycholate, 1 % Triton-X, 0.2 % SDS, completeTM protease inhibitor cocktail (Roche) and and 1 mM phenylmethylsulfonyl fluoride (PMSF, Sigma)) using the loose pestle and sonicated for 10 seconds. The lysed samples were centrifuged for 20 min at 16000 *g* and the supernatant was stored at -80°C. Total protein concentration was determined using the BCA protein assay (Pierce). Proteins were boiled for 5 min in Laemmli sample buffer before being separated at 200V for 40 min using TGX stain-free precast gels (Bio-Rad). Stain-free protein gels were activated with UV light for 5 min and then transferred to PVDF membranes (Bio-Rad) using a turbo transfer system (Bio-Rad). Membranes were blocked for 1 hr in TBST (Tris-buffered saline with 0.1 % Tween 20) supplemented with 5 % bovine serum albumin (Sigma) and then incubated overnight at 4 °C with anti-Kv1.1 primary antibody (Rb-Af400, Frontier Institute, 1:100). After primary antibody incubation, membranes were washed four times with TBST for 5 min and then incubated with anti-rabbit IRDye 800CW (LI-COR Biosciences, dilution 1:4000) for 1 hr at room temperature.

Analysis of behavioural data

Automatic image processing of the behavioural video frames identified the central position of the mouse and the heading direction. Exploratory behavioural metrics during the acclimatisation period were calculated from videos of the first 10 min mice were placed within the arena. A shelter exit was defined as an episode where the full body of the mouse moved from the inside to the outside of the

shelter. The maximum distance travelled during an exit was defined as the maximal distance reached in a straight line between the centre of the mouse and the centre of the shelter. The exit duration was defined as the time between when the full body of the mouse crossed over until it re-crossed the shelter boundary. The interbout interval during exploration was the time between subsequent shelter exits. The centre position of the mouse, [X_m, Y_m], was used to quantify the percentage of the 10 min recorded that the mouse was either outside of the shelter, in the centre of the area (defined as a circular area, centred on the centre of the arena where the loom was presented, [X_c, Y_c], with a 7 cm radius) or at the edge of the area (defined as outside of a circular area, centred on [X_c, Y_c] with a 14 cm radius).

LAR responses were assessed by analysing a peri-stimulus period starting from 3 s before the stimulus until 10 s after the stimulus onset. Responses were classified as escapes if the mouse returned to the shelter within 7 s after stimulus onset and reached a maximum speed of >20 cm s^{-1} in travelling back to the shelter. The maximum escape speed was calculated as the peak value of the speed trace between the onset of the escape and entry into the shelter. The reaction time of the mouse was calculated as the time from stimulus onset till the mouse reached the maximum speed during its escape back to the shelter. This reaction time was then used to group the responses of the animals (Figs. 1c, 6b,g & Extended Data Figs. 2b, 3b) depending on which loom presentation the peak of their escape response was recorded. The number of looms triggered is the total number of loom stimuli triggered across the 5 days of testing, not including the reward trial. The immediate speed change in response to the looming stimulus (Fig. 1d-e & Extended Data Figs. 2a, 3e-f) was calculated by paired comparisons of the average speed in the time 300-800 ms after the start of the stimulus (S_{im}) and the average speed in the peristimulus period ±50 ms around the start of the stimulus (S_{at}).

To understand the effect of certain parameters of the mouse's position and location within the arena on its LER response we calculated the distance of the mouse from shelter (defined as the straight line distance between [X_m, Y_m] and [X_s, Y_s]) and the heading angle of the mouse at the time of stimulus start (defined as the angle (BÂC) between point B, the tip of the mouse's snout, A, the position between the two back paws of the mouse and C the centre of the shelter, [X_s,Y_s]). The position of the mouse's body parts was located using DeepLabCut tracking[41]. The trajectory directedness of individual escapes was defined as (1 - (d-d_{min}/d+d_{min})), where d is the cumulative displacement of the mouse from its position at the time of the stimulus, [X_m,Y_m], start till when the centre of the mouse's body re-enters the shelter, and d_{min} is the straight line distance between [X_m, Y_m] and [X_s, Y_s]. The distance from the loom was calculated as the straight distance between the centre of the arena [X_c, Y_c], and the centre of the mouse [X_m, Y_m].

For the analysis of the response dynamics during the reward trials, only trials where the animals made a noticeable escape back to the shelter were included. Four *Setd5*$^{+/-}$ trials were removed from the final analysis because the mouse was interacting with the banana chip reward during the stimulus presentation.

For the behavioural experiments, the initial tracking and analysis of the escape behaviour were done blind through automatic analysis scripts and the genotypes were added later when pooling the animal's data together. Behaviour metrics were calculated both by pooling trials across all animals and also by calculating the average per mouse and computing an average across all mice, detailed explanations of each analysis can be found in Supplementary Table 1 and are mentioned specifically in the text.

Analysis of optogenetics experiments

Trials were pooled across animals from each genotype and psychometric curves were generated by fitting logistic regression curves to the data. The Log_{10}(**Δ**Speed) (Fig. 3l & Extended Fig. 5g) was calculated as the logarithmic of the ratio between the average speed in the time 300-800 ms after the start of the stimulus (S_{im}) and the average speed in the peristimulus period ±50 ms around the start of the stimulus (S_{at}). The data of the Log_{10}(**Δ**Speed) across laser powers was analysed using a two-way repeated measures ANOVA looking at the effect of genotype, laser power and their interaction, followed by a multiple comparisons analysis with Bonferroni correction. For the stacked bar charts, trials were grouped based on whether the speed immediately (300-800 ms) after the onset of the laser (S_{im}), was more than, less than or within 1 standard deviation from the average speed in a time window ±50 ms around light onset (S_{at}). Chi-Square tests were used to compare the distribution of all the *Setd5*$^{+/+}$ and *Setd5*$^{+/-}$ trials at different laser powers. See Supplementary Table 1 for more details.

Analysis of *in vivo* silicon probe recordings

Preprocessing. Initial analysis was performed in MATLAB R2018b and later in MATLAB R2019a. Raw voltage traces were high-pass filtered (300 Hz) and spikes were detected and sorted using Kilosort2 (https://github.com/cortex-lab/Kilosort) and Phy as previously described[46], followed by manual curation. Firing rates histograms were calculated as the average firing rate across 16.7 ms time bins. Analog input channels (Photodiode, camera trigger) were extracted in MATLAB (MathWorks, Inc.) and arduino were recorded at a 20 kHz sample rate and were used for offline synchronisation. Custom-made scripts in MATLAB were used to extract the time points of the visual stimulus onsets and matched them to the corresponding video camera frame.

Determining the surface of the superficial superior colliculus (sSC). Initial SC location was determined in real-time by auditory monitoring of multi-unit activity to a flashing stimulus and was later confirmed offline using a current source density analysis of the raw recording (see [47,48]) combined with histological reconstruction of the probe location visualised with DiI. CSD profiles were calculated for each recording and were used to align the depth of the units across recordings and across animals. The transition point between an overlying source and underlying sink was taken as the boundary between the stratum griseum superficiale (SGS) and the stratum opticum (SO). The boundary between the superficial (sSC) and intermediate/deep superior colliculus (idSC) was defined as 100 μm below this inflection depth (ID), taking into account the thickness of the SO. sSC was defined as 300 μm above the ID to 100 μm below the ID, and idSC was defined as the

area below 100 μm below the ID. Only units identified as within the sSC and units with at least 2 spikes within the stimulus presentation were used for analysis. For all analyses spikes were sorted into peristimulus periods based on synchronisation with the stimulus frames and firing-rate histograms were calculated over 16.7 ms time bins.

Analysis of baseline firing properties. Responses to a full field grey screen during the first 60s of recording were taken to determine the baseline firing properties of the recorded cells. The baseline firing rate per animal was calculated as the mean firing rate across cells in the 1000 μm below the sSC surface.

Analysis of responses to flash stimulus. Responses to a single flash stimulus (0.5 s OFF; 1 s ON; 0.5 s OFF) were generated by averaging the firing-rate histograms across 10 repetitions of the stimulus. The responsiveness of single units was defined based on the p-value generated from running a ZETA test[49] on the average firing rate histograms using the 30 s period before the stimulus as baseline and the 2 s flash stimulus as the response time. Clustering of responsive units was done using K-means and the number of clusters was determined by identifying the elbow point when analysing the Calinski-Harabasz index. Clustering was done with units from both genotypes pooled together, then later split based on genotype. The proportion of flash-responsive cells for *Ptchd1* and *Cul3* animals were determined for each animal by dividing the number of sSC units that were $p < 0.05$ by the total number of sSC units found.

Analysis of responses to loom stimulus. Responses to a single loom stimulus were obtained by averaging the responses to the first loom of the loom bout stimulus (consisting of 5 consecutive looms) across 10 repetitions. Responsiveness was again defined as units having a *p*-value (determined using the ZETA test) of < 0.05, with the 30 s preceding the loom stimulus as baseline and the 0.7 s of first loom presentation as the response time. The average firing rate was calculated as the overall average of the mean firing rate recorded across each of the 5 loom presentations individually for 10 repetitions. Maximum firing was similarly calculated as the mean maximum firing during each of the 5 looms, averaged across 10 repetitions. The time-to-peak was calculated as the mean of the time to the peak firing within each of the 5 looms, averaged over the 10 repetitions.

Analysis of responses to shifting white noise stimulus. To further analyse the visual receptive fields (RFs) of the units recorded we analysed their responses to a shifting white noise stimulus[45] and calculated them as spike-triggered averages. The location of the centre of the receptive field was estimated by finding the pixel with the highest variance over a peri-spike time period and the final RF was cropped to 160 x 160 pixels centred on this pixel with highest variance. Signal-to-noise ratio (SNR) for each neuron is defined as $10 \cdot log_{10}(max_{power}/noise_{power})$, where max_{power} is the square of the pixel value at the receptive field centre, and $noise_{power}$ the variance of all the values in a 5 pixels border around the edge of the RF. Visually-responsive neurons were defined as those with SNRs in the 80th percentile of the SNRs of all sSC units or above. The centre of the RF was assigned as ON or OFF based on the sign of the mean of the central pixel at the centre of the receptive field. The proportion of OFF RFs was calculated as the ratio between visually-responsive cells with OFF RFs and the total number of visually-responsive cells in the sSC. The radius of the RF centre was

calculated as the width at half-peak of the spatial RF profile. The average radius of the receptive fields of an animal was calculated using only the visually-responsive units. Temporal receptive fields were clustered similarly to flash responses, using K-means to cluster the responses and the number of clusters was determined using the Calinski-Harabasz index.

Analysis of responses to moving bars and gratings stimuli. For each direction the mean across trials was calculated and normalised to the baseline firing in the 30 s before stimulus onset. The preferred direction (D_p) was defined as the direction with the greatest normalised response and the non-preferred direction (D_{np}) was taken as 180 degrees from that angle. The direction selectivity index (DSI) was then computed as $(D_p-D_{np})/(D_p+D_{np})$ with values falling in a range from 1 (high direction selectivity) to 0 (low direction selectivity). Units were defined as being 'direction selective' (DS) if their DSI was in the 80th percentile or higher out of all units recorded within the sSC. The proportion of direction selective cells per animal was found by quantifying the proportion of DS sSC units divided by all sSC units recorded for that animal.

Analysis of behavioural data from head-fixed visual stimulation. The motion of the animal was determined by sorting the difference between pixels in neighbouring frames with K-means into two groups. The proportion of time each animal spent running was calculated as the proportion of frames that were registered as 'moving' over the total number of frames. The pupillary light reflex (PLR) of the animals was assessed by tracking the change in pupil size across the repetitions of the flash stimulus. A deep neural network approach for markerless tracking[50] was used to extract points around the pupil. The diameter of the pupil was then calculated by fitting an ellipse to these points. Since we observed, and it is known, that the size of the pupil is greatly affected by locomotion, when analysing the PLR we only included repetitions in which the mice were running. An animal was considered to be running during a repetition if the mouse was classified as 'moving' in over half of the video frames covering that repetition.

Analysis of in vitro patch clamp electrophysiological recordings

Whole-cell recordings were analysed in Clampfit (Molecular Devices) and MiniAnalysis Program (Synaptosoft). Resting membrane potential (RMP) was measured as the average membrane potential prior to current-injection. Input resistance (R_{in}) was calculated from the slope of the linear fit of the hyperpolarising current/voltage relationship. Membrane time constant τ was measured from the exponential fit of the membrane potential change in response to a –10 or –20 pA current-injection. Membrane capacitance (C_m) was calculated from $C_m = \tau/R_{in}$. Action potential firing was quantified in Clampfit using the event detection function. Phase-plane plots were performed to investigate the dynamic changes in the membrane potential over time (dV/dt) and were generated using the spikes from the first current step necessary to elicit action potentials (rheobase current). Soma size was calculated by fitting an oval to the projected image (63X) of the neurons and calculating the area of that oval.

Analysis of cannula experiments

Trials were pooled across animals from each genotype. The reaction time and maximum escape speed were calculated from evoked escape responses. Responses were classified as escapes based on the same criteria used in the standard LER trials. Shelter exits were quantified as the average number of shelter exits per animal over the LER trials either with saline or with α-DTX. Comparisons of *Setd5*$^{+/+}$ or *Setd5*$^{+/-}$ animals with saline versus α-DTX were done with paired *t*-tests if the data reached the normality criteria, otherwise paired Wilcoxon's rank sum tests were used. Unpaired Wilcoxon's rank sum tests were used for comparisons across genotypes. See Supplementary Table 1 for more details.

Analysis of histological data

For comparison between the Kv1.1 expression in *Setd5*$^{+/+}$ and *Setd5*$^{+/-}$ tissue 30 μm stacks were imaged with 1 μm sections at 63X magnification, or 55 μm stacks were imaged with 2 μm sections at 20X magnification, and the same laser power settings were used for all images at a given magnification.

Analysis of western blot data

The Bio-Rad ChemiDoc MP system was used for imaging and acquisition and images were quantified using ImageJ software. Protein levels are displayed as fold change. Student's *t-test* was used to test for significance (MATLAB, MathWorks, Inc.). Data represent mean ± SEM obtained from three mice per genotype.

Statistics

Analyses were performed in custom-written MATLAB (2019a) scripts (MathWorks, Inc.). Shapiro-Wilk and Levene's tests were used to test the normality and the equal variances of the datasets, respectively and were parametric or non-parametric tests used accordingly. Two-tailed tests were used unless specified. All statistical tests are reported in the text and appropriate figure legends ($^{*}p < 0.05$, $^{**}p < 0.01$, $^{***}p < 0.001$). In bar plots, the mean ± s.e.m. are shown, unless otherwise stated. Boxplots display the median and IQR. Please see Supplementary Table 1 for a detailed statistical analysis.

Data and code availability

Behavioural data, *in vivo* electrophysiological silicon probe data and *in vitro* electrophysiological patch clamp data will be deposited and made available as of the date of publication. DOIs will be listed in the key resources table. Microscopy data reported in this paper will be shared by the lead contact upon request.

All original code will be deposited and made publicly available as of the date of publication.

Any additional information required to reanalyze the data reported in this paper is available from the lead contact upon request.